SANDIA REPORT

SAND2012-8980
Unlimited Release
Printed October 2012

Field-theoretic Simulations of Block Copolymers: Design and Solvent Annealing

Sean Paradiso, Glenn H. Fredrickson, Edward H. Feng, and Amalie L. Frischknecht

Prepared by
Sandia National Laboratories
Albuquerque, New Mexico 87185 and Livermore, California 94550

Sandia National Laboratories is a multi-program laboratory managed and operated by Sandia Corporation, a wholly owned subsidiary of Lockheed Martin Corporation, for the U.S. Department of Energy's National Nuclear Security Administration under contract DE-AC04-94AL85000.

Approved for public release; further dissemination unlimited.

Sandia National Laboratories

Issued by Sandia National Laboratories, operated for the United States Department of Energy by Sandia Corporation.

NOTICE: This report was prepared as an account of work sponsored by an agency of the United States Government. Neither the United States Government, nor any agency thereof, nor any of their employees, nor any of their contractors, subcontractors, or their employees, make any warranty, express or implied, or assume any legal liability or responsibility for the accuracy, completeness, or usefulness of any information, apparatus, product, or process disclosed, or represent that its use would not infringe privately owned rights. Reference herein to any specific commercial product, process, or service by trade name, trademark, manufacturer, or otherwise, does not necessarily constitute or imply its endorsement, recommendation, or favoring by the United States Government, any agency thereof, or any of their contractors or subcontractors. The views and opinions expressed herein do not necessarily state or reflect those of the United States Government, any agency thereof, or any of their contractors.

Printed in the United States of America. This report has been reproduced directly from the best available copy.

Available to DOE and DOE contractors from
U.S. Department of Energy
Office of Scientific and Technical Information
P.O. Box 62
Oak Ridge, TN 37831

Telephone: (865) 576-8401
Facsimile: (865) 576-5728
E-Mail: reports@adonis.osti.gov
Online ordering: http://www.osti.gov/bridge

Available to the public from
U.S. Department of Commerce
National Technical Information Service
5285 Port Royal Rd
Springfield, VA 22161

Telephone: (800) 553-6847
Facsimile: (703) 605-6900
E-Mail: orders@ntis.fedworld.gov
Online ordering: http://www.ntis.gov/help/ordermethods.asp?loc=7-4-0#online

SAND2012-8980
Unlimited Release
Printed October 2012

Field-theoretic Simulations of Block Copolymers: Design and Solvent Annealing

Sean Paradiso and Glenn H. Fredrickson
Department of Chemical Engineering
University of California, Santa Barbara
Santa Barbara, CA 93106

Edward H. Feng and Amalie L. Frischknecht
Sandia National Laboratories
Livermore, CA 94550 and
Albuquerque, NM 87185

Abstract

We first propose a solution to the inverse design problem for block copolymers that uses self-consistent field theory (SCFT) with numerical optimization. We apply our design methodology to both conformationally symmetric and asymmetric diblock copolymer melts. In the latter case, the parameters are specific to poly(ethylene oxide-b-styrene) block copolymer (PEO-PS), a material currently being explored as an electrolyte for lithium-ion batteries. The results of this design approach not only guide the synthesis of block copolymers but also shed light on the polymer physics of the gyroid phase. Second, we develop an SCFT to isolate and study the dynamical aspects of micro-phase separation in block copolymer films during the film drying process. Key questions include whether evaporation rate as a controlled, independent variable can effect a change in micro-domain orientation, whether a concentration-dependent kinetic mobility is required to explain such an effect, and working out the consequences for controlling the morphology alignment in copolymer films of varying thicknesses.

Acknowledgments

This work was part of the LDRD project “Triblock Polymers for Nanoporous Membranes”. E.H.F. thanks Paul Boggs for his insights into optimization, and Nate Lynd, Amalie Frischknecht, and Joseph Cordaro for useful conversations. S. P. thanks Kris Delaney, Su-Mi Hur, Carlos Garcia-Cervera, and Hector Ceniceros for helpful discussions.

Contents

Preface **10**

1 Designing Block Copolymer Materials **11**

1.1 Introduction 11

1.2 Methods 12

1.3 Results 14

1.4 Discussion 15

1.5 Outlook 17

1.6 Appendix: Rescaling Monomer Volume 17

2 Features of Evaporation-Induced Ordering in Block Copolymer Thin Films **21**

2.1 Introduction and Background 21

2.1.1 Morphology Control via Solvent Annealing 22

2.2 Theoretical Framework 23

2.2.1 Polymer Model 23

2.2.2 Field Theory Formulation 24

2.2.3 Dynamics 25

Modeling Evaporation 25

Concentration Dynamics Equations 26

Evaluating the Thermodynamic Force 28

2.2.4 Summary of Equations for the Current System 29

2.3 Numerical Solution 30

2.3.1 Discretized Dynamics Equations 30

Numerical Solution 32
2.3.2 Simulation Details 33
Size Considerations: Polymers and Point Particles 33
Choosing Thin Film Parameters 34
2.4 Results 35
2.4.1 Evaporation-Induced Ordering Fronts: Symmetric Copolymer Case 35
Non-Local Effects Due to Bonded Interactions 35
2.4.2 Evaporation-Induced Ordering Fronts: Asymmetric Copolymer Case 37
Sweeping for Neutral Surface Conditions 38
Evaporation Rate Effects 39
References 42

List of Figures

1.1 Free energy of three candidate phases as a function of f at $\chi N = 15$ for a conformationally symmetric diblock copolymer. The arrow shows that the free energy of the gyroid phase is furthest below the other two phases at $f \approx 0.392$, a result determined from SCFT and optimization. At this optimal point, the lamellar and hexagonally packed cylinder phase have the same free energy. 13

1.2 Results for both conformationally symmetric $\alpha = 1.0$ and asymmetric $\alpha = 1.44$ diblock copolymer melts. Part (a) shows the free energy difference per monomer volume between the gyroid and the lamellar and hex phases as a function of χN. The $\alpha = 1.0$ and $\alpha = 1.44$with$f < 0.5$ display a minimum which corresponds to the optimal point in parameter space. This point is denoted by the larger symbol. Part (b) shows the optimal block fraction f as a function of χN. 19

2.1 Typical profile of equilibrated thin film. Copolymer densities shown along with confining substrate/surface profiles. In this example f=0.4, χN_{AB}=10 and ζN = 1000. 27

2.2 Left: Film thickness as a function of simulation time (semi-log) for various evaporation rates k=-1 (top), -2, -3, -4, and -5 (bottom). The behavior at intermediate times is observed to be approximately exponential. Right: A linear fit to this region yields an exponential decay rate which is plotted vs the reaction rate parameter k. The film deswelling rate is then found to be related to the reaction rate parameter k as $L(t;k) \approx L_0 \exp(.0007k)$. 28

2.3 Typical polymer (top) and solvent (bottom) density profiles over the course of a simulation at standard, neutral conditions: $\chi N_{ASub} = \chi N_{BSub} = \chi N_{ASurf} = \chi N_{BSurf} = 1.0$, $\chi N_{SSurf} = \chi N_{SSub} = 3.0$ and k=-1.0 (A) and k=-7.0 (B). Profiles may be compared with the molecular dynamics result in reference [34] (C). 34

2.4 Typical ordering front in a symmetric (f=0.5) block copolymer thin film initially swollen with $\overline{\phi}_S(0)$=$\frac{1}{V(0)}\int \rho_S(\mathbf{r},0)d\mathbf{r}$=0.6, which corresponds to a disordered state. Strength of AB interactions and evaporation rate constant are provided in the titles of each subfigure. An $L_\perp$ front is seen to form near the free surface and extend into the film. Periodically, a splitting event is observed which is tentatively attributed to the non-local nature of the thermodynamic forces, discussed in the text. 36

2.5 Illustration of how the copolymer fluid orders at the interface between an $L_\perp$ front and the disordered bulk film. The inset zooms in on this region, where the linear fluid response is indicated by dashed chains which orient to match the tails protruding from the caps of the lamellae. Essentially, blue stripes have red tails, attracting red tails from the disordered fluid, resulting in slight enrichment of blue tails just below that. Neighboring stripes exhibit analogous, inverted behavior (red-blue-red) which sets up a checker board layer below the ordering front. 37

2.6 Saddle-point solutions converged using standard Self-Consistent Field Theory methods. The disordered region in the bottom half of the cell is maintained by masking the bottom region to maintain the total polymer density $\rho_A(z < 10) + \rho_B(z < 10)$=0.5 while $\rho_A(z \geq 10) + \rho_B(z \geq 10)$=1.0. In the dilution approximation, this leaves χN_{eff}=10 (left) and χN_{eff}=10.5 (right). At the ODT, the half-period shifted region is seen to extend to the rest of the cell, while below the ODT (left) the checkerboard pattern is observed in the viscinity ∼2Rg of the interface. 38

2.7 Heat maps showing the value of a perpendicular order parameter at the end of each simulation (when the remaining solvent fraction was less than 0.05). Perpendicular order is given as the sum of any contributing modes in the Fourier transform of the final morphology with $k_x \neq 0$ where x denotes the axis running parallel to the substrate, ie. $\psi = \sum_{k_x \neq 0} \widehat{\rho}(\mathbf{k})$. Notice that the region of perpendicular order grows between k=-2.5 and k=-3.5, but shows no further improvement with increasing evaporation rate. The surface disappears completely for evaporation rates below k=-2.0, indicating a minimum required evaporation rate to initiate a perpendicular ordering front. 39

2.8 Comparison between successful nucleation of a perpendicular ordering front and a simulation whose conditions were outside the region of perpendicular order indicated in figure 2.7. Both simulations exhibit a slight $L_\parallel$ wave from the surface along with slight "post" formation at the surface. In the failed (bottom) trajectory, the preferentiality of the surface succeeded in damping the post formation, leading to parallel morphology. Time increases left→right, successful trajectory is in row 1, unsuccessful trajectory (k=-2.5) in row 2. 41

List of Tables

1.1 For diblock copolymer melts, these are the optimal parameters at which the gyroid phase is most stable. Here, $\alpha = a_A/a_B$ characterizes the conformational asymmetry of the diblock copolymer, f is the fraction of the A block, and χN is the product of the Flory-Huggins parameter and polymer length. 15

Preface

This report presents work done under the LDRD project, "Triblock Polymers for Nanoporous Membranes". The final SAND report for that project can be found as: Joseph G. Cordaro, Nicolas R. Myllenbeck, Matthew C. George, Michael S. Kent, Amalie L. Frischknecht, Geoffrey Brennecka, Greg OBryan, and Edward H. Feng, "Triblock Polymers for Nanoporous Membranes", Sandia National Laboratories Report SAND2012-7479 (2012).

In this report, we present results from two computational studies that were done to support the main experimental work. Both studies use a standard theory for describing the phase behavior of block copolymer melts, the self-consistent field theory (SCFT) [11]. Chapter 1 presents the results of an examination of whether optimization methods can be used in conjunction with SCFT calculations to design a particular desired block copolymer; this was work performed by Edward H. Feng. Chapter 2 describes work by Sean Paradiso and Glenn H. Fredrickson at U. C. Santa Barbara, who have developed a new technique for describing solvent annealing within SCFT. They then apply this method to examine the effects of solvent annealing on ordering in diblock copolymer thin films.

Chapter 1

Designing Block Copolymer Materials

1.1 Introduction

Over the last 17 years, the polymer physics community has made great strides in using computational self-consistent field theory (SCFT) [23, 12, 11] to understand the self- assembly of block copolymers. For a diblock copolymer with parameters that describe the architecture of the copolymer and interaction between the monomer species, SCFT determines the phase into which this copolymer will self-assemble. However, an engineer desires to make a material with a particular structure, such as the bicontinuous structure of the gyroid phase. With this endpoint in mind, the engineer wants to know which block copolymer to make. If SCFT provides a solution to the forward problem that takes polymer parameters to self-assembled phase, the engineer needs a solution to the inverse problem that maps phase to polymer parameters. Useful predictions include the mass of both blocks of the copolymer and the temperature at which to anneal the system.

Researchers in the theoretical community have considered this inverse design problem in other systems. Stillinger, Torquato and coworkers developed a potential function that makes atoms crystallize into a desired structure [29, 32]. They use simulated annealing to determine the optimal potential for the diamond structure with useful band gap properties. This work inspired mathematicians to develop a linear programming algorithm to find the potential that optimizes a zero temperature ground state [6]. Beratan, Yang and coworkers also use optimization to design molecules with high polarizability [38] as well as protein sequences that fold into a desired structure [15]. However, to our knowledge, no one has designed block copolymers that self-assemble into a desired microstructure.

Here, we propose a solution to the inverse design problem for block copolymers that uses SCFT with numerical optimization. This solution is based on an objective function proportional the free energy difference between the target and other candidate phases. Optimization of this function maximizes the thermodynamic driving force towards the target phase. While one could choose any target phase, we consider the gyroid phase since its bicontinuous structure gives a material with the properties of both polymers. We apply this design methodology to both conformationally symmetric and asymmetric diblock copolymer melts. In the latter case, the parameters are specific to poly(ethylene oxide-b-styrene) block copolymer (PEO-PS), a material currently being explored as an electrolyte for lithium-ion batteries. The results of this design approach not only guide the synthesis of block copolymers but also shed light on the polymer physics of the gyroid phase.

1.2 Methods

Self-consistent field theory (SCFT) [11] uses statistical mechanics to predict the self-assembly of block copolymers at thermal equilibrium. It accounts for the chemical incompatibility between different monomer species, the configurational entropy of the polymer chains and the incompressibility of a polymer liquid. One formulates the field theory in terms of the chemical potential fields conjugate to the monomer densities and then makes a mean field approximation. Computational methods are used to find the mean field solution for different candidate phases such as lamellae, hexagonally packed cylinders and gyroid phases.

Many researchers have provided a complete theoretical description of SCFT [23, 11], so we restrict our attention to those aspects crucial to the design results. Consider a diblock copolymer melt in the canonical ensemble with n polymers of length N in a volume V at a temperature T. Each copolymer has blocks of A and B monomers that consume a volume fraction f and $1-f$ of the polymer respectively, and the Flory-Huggins parameter χ describes the chemical incompatibility of the two blocks. The heart of the SCFT calculation solves a modified diffusion equation

$$\frac{\partial q(\mathbf{r},s)}{\partial s} = \begin{cases} \frac{1}{6}Na_A\nabla^2 q(\mathbf{r},s) - w_A(\mathbf{r})q(\mathbf{r},s), & s < fN \\ \frac{1}{6}Na_B\nabla^2 q(\mathbf{r},s) - w_B(\mathbf{r})q(\mathbf{r},s), & s > fN \end{cases} \tag{1.1}$$

for the propagator $q(r,s)$ with the boundary condition $q(r,0) = 1$ at the A end of the block copolymer. Here, r is the position in space, and the contour variable $s \in [0,N]$ describes the N monomer volumes v_0 along the chain. Moreover, $w_i(\mathbf{r})$ and a_i are the chemical potential fields and Kuhn lengths for the i = A, B monomer species respectively. For a set of fields $w_A(\mathbf{r})$ and $w_B(\mathbf{r})$, solving the modified diffusion equation leads directly to the inhomogeneous spatial distribution in an ordered phase,

$$\phi_A(\mathbf{r}) = \frac{1}{Q}\int_0^{fN} q(\mathbf{r},s)q^\dagger(\mathbf{r},s) \tag{1.2}$$

Here,

$$Q = \frac{1}{V}\int q(\mathbf{r},N)d\mathbf{r} \tag{1.3}$$

is the dimensionless single chain partition function for a polymer in chemical potential fields $w_A(\mathbf{r})$ and $w_B(\mathbf{r})$, and the propagator $q^\dagger(\mathbf{r},s)$ arises from solving the modified diffusion equation starting from the B end of the block copolymer. If one multiplies the left side of Eq. (1.1) by -1, this propagator satisfies this equation with the boundary condition $q^\dagger(\mathbf{r},s) = 1$. The volume fraction for the B monomers is similar to Eq. (1.2) except with a change in the limits of integration so the contour integral includes the B block of the polymer.

With the ability to solve for the densities given the fields, we can find the $w_A(\mathbf{r})$ and $w_B(\mathbf{r})$ fields that satisfy a set of mean field equations.[11] If $w_A^*(\mathbf{r})$ and $w_B^*(\mathbf{r})$ are these mean field solutions, the free energy in the canonical ensemble with n polymers in a volume V at temperature T is

$$\frac{F[w_A^*, w_B^*]}{nkT} = -\frac{\chi N}{V}\int \phi_A(\mathbf{r})\phi_B(\mathbf{r})d\mathbf{r} - \ln Q \tag{1.4}$$

in which the Flory-Huggins parameter χ is in units of kT and k is Boltzmanns constant. For a conformationally symmetric diblock copolymer in which $a_A = a_B$, we show this free energy for

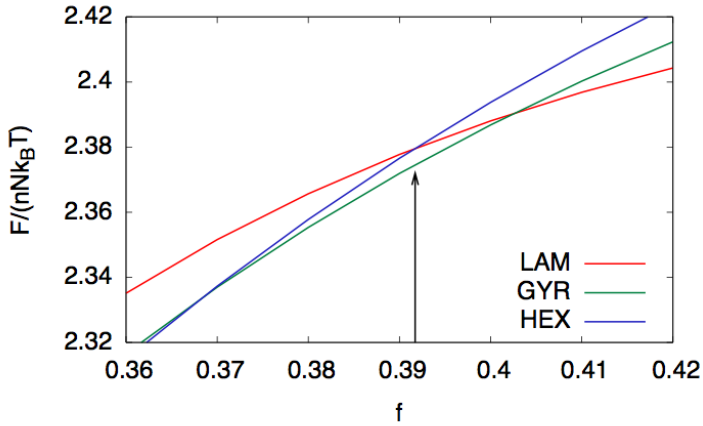

Figure 1.1. Free energy of three candidate phases as a function of f at $\chi N = 15$ for a conformationally symmetric diblock copolymer. The arrow shows that the free energy of the gyroid phase is furthest below the other two phases at $f \approx 0.392$, a result determined from SCFT and optimization. At this optimal point, the lamellar and hexagonally packed cylinder phase have the same free energy.

the lamellar, gyroid and cylinder phases as a function of f at $\chi N = 15$ in Fig. 1.1. The standard block copolymer phase diagram1 is constructed by finding the phase of lowest free energy at all values of f and χN.

To design polymeric materials, we assume the target phase is most stable when its free energy is furthest below the free energy of all other phases. This point in parameter space maximizes the thermodynamic driving force towards the target phase. For a diblock copolymer melt, this requires finding the f and χN at this maximum. To formulate this as an optimization problem, let Θ be the set of parameters for the block copolymer system. For a diblock copolymer melt, $\Theta = \{f, \chi N\}$ but the size of this set grows as monomer and polymer species are added to the system. For example, a triblock copolymer has 5 independent parameters, a size that already makes calculating the full phase diagram tedious. Let $F_T(\Theta)$ be the free energy of the target phase and $F_j(\Theta)$ be the free energy of all other phases $j = 1...N$. We assume $F_j(\Theta)$ and $F_T(\Theta)$ are continuous and differentiable with respect to each element of Θ. The curves in Fig. 1.1 support this assumption. Consider the function

$$J(\Theta) = \min_j \left(F_j(\Theta) - F_T(\Theta)\right), \tag{1.5}$$

the difference between the free energy of the lowest non-target phases and the target phase. Since we only desire solutions in which the target phase has the lowest free energy, we seek the solution to

$$\max_{\Theta} J(\Theta), \quad \text{subject to } J(\Theta) \geq 0 \tag{1.6}$$

This optimization scheme is similar to the zero temperature scheme4 that Rechtsman et al. applied to crystal structures. With the gyroid as the target phase for the diblock copolymer in Fig. 1.1,

$J(\Theta)$ reaches its maximum at $f \approx 0.392$. However, this objective function is not differentiable everywhere. In fact, $J(\Theta)$ is not differentiable at its maximum since the identity of the phase of next lowest free energy changes. This potentially makes it difficult to use optimization codes employing gradient methods.

We propose an alternative formulation [25] of the problem. Consider the free energy differences $F_j(\Theta) - F_T(\Theta)$. If these are all greater than some threshold $s > 0$, then it suffices to maximize the scalar value s. For the constraints

$$g_j(\Theta, s) = F_j(\Theta) - F_T(\Theta) - s \tag{1.7}$$

we solve

$$\max_{\Theta, s} \quad \text{subject to} \begin{cases} g_j(\Theta, \mu) \geq 0, & \forall j \\ s \geq 0 \end{cases} \tag{1.8}$$

This optimization problem has a simple objective function and nonlinear constraints. Since we assume$F_j(\Theta)$ is differentiable with respect to each element in Θ for all j, then each constraint $g_j(\Theta, s)$ is also differentiable with respect to all its parameters.

To implement this design scheme, we use the SCFT code developed by the Morse group [1]. We consider diblock copolymer melts and adopt the original Matsen-Schick formulation [23] in which $N = 1$ and a block copolymer occupies a single monomer volume. Taking the parameters $\chi = \chi N$ and f as inputs, the SCFT code performs a unit cell calculation based on the symmetries of the phase by solving Eq. (1.1) in Fourier space. We use a spatial resolution of at least 483 (1175 basis functions) for the gyroid phase, sufficient accuracy [21] for our calculations in which $\chi N \leq 30$. The design method targets the gyroid phase. From previous work on block copolymer phase diagrams [23, 35], it suffices to consider only the neighboring lamellar and cylinder phases in this calculation. The DAKOTA package [2] works with SCFT to find the optimal point in parameter space. It implements a sequential quadratic programming algorithm [25] through the NPSOL package, calculates numerical gradients and terminates when the change in the objective function divided by its magnitude is less than 10^{-4}, the default option in DAKOTA. With sufficient accuracy in calculating free energy of the gyroid phase, DAKOTA had no problems converging to the optimal parameters for the systems studied.

1.3 Results

First, we consider a conformationally symmetric diblock copolymer in which the two species have equal Kuhn lengths $a_A = a_B$. To begin, we fix χN = 15 and perform a one dimensional optimization in the parameter f. Our method gives f = 0.392, a result depicted in Fig. 1.1. At this optimal point, the free energy of the neighboring lamellar and cylinder phases have the same value. Both of the inequality constraints in Eq. 1.7 are equalities, or are active, at the optimal point, a feature present at all optimal parameters in this work. Next, we perform a two dimensional optimization in f and χN that searches the entire phase diagram of a block copolymer melt. Starting at f = 0.44 and χN = 15, this calculation converges to f = 0.352 and χN = 23.65. Since the initial point is far away

from the optimal point, the sequential quadratic programming algorithm appears to have a large radius of convergence.

Next, we consider a conformationally asymmetric diblock copolymer in which $\alpha = a_A/a_B = 1.44$. This parameter choice corresponds to a PEO-PS system14 in which the A block is the more flexible PEO. When $f < 0.5$, the optimal parameters are $f = 0.414$ and $\chi N = 23.71$. These results are consistent with phase diagrams for asymmetric diblocks [21] in which the gyroid phase shifts to higher values of f as α increases. The flexibility of the minority component alleviates packing frustration and causes the interface to curve towards the minority phase. For $f > 0.5$, the optimal parameters are $f = 0.716$ and $\chi N = 30.0$, a point at the upper limit of χN values in our calculation. A summary of these results are given in Table 1.1.

Table 1.1. For diblock copolymer melts, these are the optimal parameters at which the gyroid phase is most stable. Here, $\alpha = a_A/a_B$ characterizes the conformational asymmetry of the diblock copolymer, f is the fraction of the A block, and χN is the product of the Flory-Huggins parameter and polymer length.

α	f	χN
1.00	0.352	23.65
1.00	0.648	23.65
1.44	0.414	23.71
1.44	0.716	23.71

To compare these three systems, we plot the free energy difference between the gyroid phase and the phase with the next highest free energy as a function of χN in Fig. 1.2a. Each datum in this plot corresponds to an optimization for f at a fixed χN, the same calculation used to find the optimal $f = 0.392$ in Fig. 1.1. Larger negative values correspond to a more stable gyroid phase. At each data point, the lamellar and hexagonal packed cylinder phases have the same free energy. Hence, each data point corresponds to the metastable cylinder lamellae boundary, and Matsen [21] calculated the results in Fig. 1.2a for $\alpha = 1.5$. For the diblock with the more flexible majority component, there may be a minimum for $\chi N > 30$. Calculations with more basis functions for the gyroid phase could resolve this issue.

1.4 Discussion

Approaching the study of block copolymers from a design perspective can also shed new light on the self-assembly of complex phases like the gyroid. Previous work has shown that phase selection, or what phase is most stable at a point in the phase diagram, is a delicate balance between the interfacial tension and packing frustration [7]. The enthalpic interaction parametrized by χN drives the formation of interfaces with constant mean curvature. Meanwhile, the entropy loss associated with chain stretching makes it more difficult for chains to pack efficiently and hence distorts these

constant curvature interfaces. The gyroid phase is stable in the block copolymer phase diagram because the shape of its interface lessens the packing frustration compared with other complex phases such as perforated lamellar and double diamond. Fig. 2a shows that conformational asymmetry further stabilizes the gyroid phase, since the free energy gap to the next highest phase is larger for $\alpha = 1.44$ than $\alpha = 1$. The more flexible A blocks lessens the packing frustration in this system. This is not true when the more flexible block composes the majority domain for $\chi N \geq 30$, as this free energy difference is always larger than other two systems.

To see how these computational results translate into guidelines for polymer synthesis, consider a PEO-PS block copolymer. With PEO and PS as the minority and majority block respectively, this system15 corresponds to calculations with $\alpha = 1.44$ and $f < 0.5$. To make the connection with experiments, we use literature values [22] for the Flory-Huggins parameter $\chi(T) = -1.73 \times 10^{-2} + 23.7T^{-1}$ which depends on the interpretation of N as the number of $v_0 = 0.1$ nm^3 monomer volumes occupied by the diblock copolymer. The appendix shows how to change variables from our SCFT calculation to this experimental system by rescaling the monomer volume. To predict the optimal conditions for the self-assembly of the gyroid phase, we have some latitude in choosing an equilibration temperature T and polymer length N. We choose T = 180°C, which is lower than the T = 200°C at which PS-PEO begins to degrade but high enough to enhance the kinetics of self-assembly. This gives $\chi = 0.035$, which implies N = 677.4. To transition from monomer volumes to polymer molecular weight, we need the molecular weight (44 and 104 g/mol) and monomer volumes (0.069 and 0.179 nm3) of ethylene oxide and styrene respectively. Then the polymer molecular weight is $Nf_i m_i (v_0/v_i)$ in which f_i is the block fraction, m_i is the monomer mass in grams per mole, and v_i is the volume occupied by a monomer as i indexes both monomers. This gives polymer molecular weights of 17.8 and 23.0 kg/mol for PEO and PS respectively; this diblock copolymer is predicted to optimally self-assemble at T = 180°C into the gyroid phase.

Often times, domain spacing of the resulting material is of interest. The optimal PEO-PS diblock gives a domain spacing of 67.5 nm, a straightforward exercise using the change of variables in the Appendix. If a larger domain spacing is desired, one can still use the optimal solution χN = 23.71 but change χ and N accordingly. A higher equilibration temperature T = 200°C implies a smaller value of χ and hence a larger value of N at χN = 23.71. This implies a domain spacing of 70.67 nm, a small increase. However, in Fig. 2a, the free energy difference for $\alpha = 1.44$ and f ¡ 0.5 is relatively flat as χN increases beyond the optimal value of χN = 23.71. Moreover, Fig. 2b shows that the optimal block fraction stays constant as χN increases. This suggests that longer PEO-PS block copolymers with f = 0.414 might also readily self-assemble into the gyroid phase. Preliminary experimental results on this system support this assertion.

In applying this design approach to experiments, the uncertainty in parameters such as χ and a_A, a_B will affect the accuracy of the predictions. Experimental values for χ are usually obtained from analyzing scattering data on blends of two homopolymers with the random phase approximation [22]. Not only can both theory and experiment lead to errors, the analysis also makes assumptions, such as the independence of χ from the volume fractions of the two polymer species. Also, values of the Kuhn lengths a_i have been reported to vary by 20% [22]. With these uncertainties, we dont always expect quantitative accuracy with our design scheme. Nonetheless, it can certainly guide materials design better than any trial and error approach.

1.5 Outlook

Our method for designing polymeric materials is not limited to diblock copolymer melts. With the interest in using PEO-PS as a electrolyte for lithium ion batteries [13], one could study how lithium salts of various molecular volumes changes the phase behavior of PS-PEO. Instead of calculating entire phase diagrams, our method could be used to optimize the thermodynamic driving force towards the gyroid phase, whose bicontinuous structure is ideal for harnessing both the conductivity of Li in PEO as well as the mechanical stability of PS. Another topic of interest is blending homopolymer with diblock copolymers, a method that stabilizes different bicontinuous phases such as the double diamond [20]. With the inclusion of more candidate phases than the three used here, one could optimize the block fractions and polymer fractions for these other phases. Also, the design approach is applicable to multi-block copolymers with more than two blocks. With the explosion of possible phases that might be stable at any point in parameter space, one should first employ physical intuition to select candidate phases that might be stable in any particular region.

This work focuses on designing polymeric materials with self-consistent field theory, a well studied approach for the self-assembly of block copolymers. Within the mean-field approximation, the calculation gives a precise value for the free energy which leads to continuous and differentiable curves as a function of the parameters. Hence, we can use gradient based optimization methods such as sequential quadratic programming to design materials. However, other methods for calculating the free energy use stochastic methods, which leads a sampling error in the free energy estimate. For example, Lennon et al. employed complex langevin sampling to go beyond the mean-field approximation in field theoretic models of block copolymers [20]. While gradient based methods may not work, the overall design approach presented here is still useful. In the presence of sampling error, one can use stochastic programming as a means for optimization and designing materials.

1.6 Appendix: Rescaling Monomer Volume

We show that the monomer volume, Flory-Huggins parameter, degree of polymerization, and Kuhn length can be rescaled such that the field-theoretic model of block copolymers remains the same. Here, we let a denote a Kuhn length, which could arbitrarily be set to the Kuhn length of either monomer species. Suppose we rescale the monomer volume $\bar{v}_0 = \lambda v_0$. Then $\bar{\chi} = \lambda\chi$ gives the same expression for the internal energy associated with chemical incompatibility (see eq. 18 or 21 in the Fredrickson review article [12]). To ensure the same effective repulsion between chains $\bar{\chi}\bar{N} = \chi N$, we rescale the polymer length $\bar{N} = \lambda^{-1}N$. Finally, the length scale set by the squared end-to-end distance $\bar{N}\bar{a}^2 = Na^2$ remains invariant if $\bar{a} = \sqrt{\lambda}a$. This implies

$$\frac{\bar{a}^2}{\bar{v}_0} = \frac{a^2}{v_0} \tag{1.9}$$

must hold for the physics to remain invariant.

To connect the design method results with experiments, let the original and overbar variables correspond to SCFT and experiments respectively. The optimal χN value depends on an SCFT calculation in which the monomer volume was equal to the polymer volume, or $N = 1$. We seek the corresponding experimental parameters $\bar{\chi}$ and $\bar{N}$. The Flory-Huggins parameter $\bar{\chi} \ll 1$ and Kuhn length $\bar{a}$ are dictated by literature values [22]. Then $\bar{\chi}\bar{N} = \chi N$ and $N = 1$ imply a large degree of polymerization $\bar{N} \gg 1$ for the experimental system and $\lambda = 1/\sqrt{\bar{N}} \ll 1$. Hence, the rescaled monomer volume decreases as expected. To complete the analysis from above, we would use the literature value $\bar{a}$ and set $a = \bar{a}/\sqrt{\lambda}$ to make the length scale and domain spacing $\bar{d} = d$ the same in simulation and experiment. However, we set $a = \bar{a}$ in our simulation, which implies $\sqrt{Na^2} = \sqrt{\bar{N}\bar{a}^2}/\sqrt{\lambda}$ for the length scale. Hence, $\bar{d} = d/\sqrt{\lambda}$.

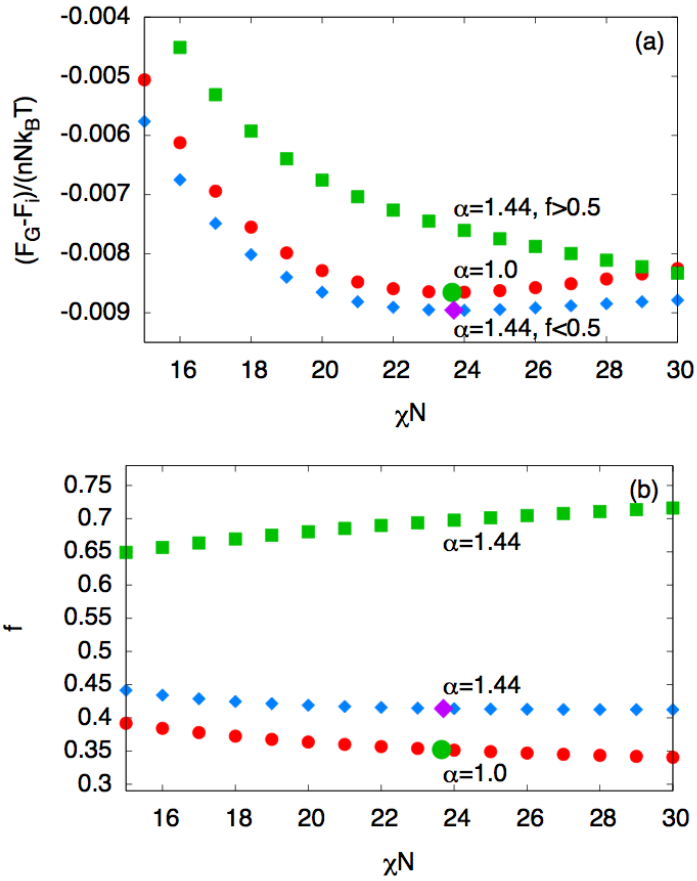

Figure 1.2. Results for both conformationally symmetric $\alpha = 1.0$ and asymmetric $\alpha = 1.44$ diblock copolymer melts. Part (a) shows the free energy difference per monomer volume between the gyroid and the lamellar and hex phases as a function of χN. The $\alpha = 1.0$ and $\alpha = 1.44$with$f < 0.5$ display a minimum which corresponds to the optimal point in parameter space. This point is denoted by the larger symbol. Part (b) shows the optimal block fraction f as a function of χN.

Chapter 2

Features of Evaporation-Induced Ordering in Block Copolymer Thin Films

2.1 Introduction and Background

The propensity for block copolymer materials to form ordered structures on tunable length scales makes them extremely attractive platforms for nanotechnology applications. In neat diblock copolymers, this micro-phase separation behavior can be successfully mapped to two parameters: the relative number of monomers comprising one block with respect to the other (block fraction), and the mean-field segregation strength χN. For sufficiently high segregation strength, sweeping through block fraction will produce first spherical micelles in a majority matrix, followed by hexagonally packed cylindrical micelles, a bicontinuous phase, and, finally, a lamellar phase at equal block fraction [10]. While a great deal of effort has been invested in understanding and leveraging self-assembly in bulk copolymer materials, recent interest has been growing in thin film materials for their unique potential for important technological areas such as membrane separations [28, 36], fuel cell proton-exchange membranes, organic photovoltaics [37], optically active coatings, and more.

For these reasons, there is great interest in the thin film community in understanding how to align block copolymer micro-structures with respect to the film surface. For some applications, such as templating nano-wires, the objective is to form straight lines of perpendicular lamellae ($L_\perp$) or a single layer of parallel cylinders ($C_\parallel$). For templating wires that break the plane, nano-scale posts, or pores for functional membranes, cylinders oriented perpendicular to the plane of the substrate are required ($C_\perp$). It has been demonstrated repeatedly that neutral free surfaces ($\Delta\gamma = 0$) promote perpendicular order close to the walls in lamellar systems [8, 30, 31]. For asymmetric, cylinder-forming systems the surface field is not quite as clear, as enthalpically neutral surfaces (a condition enforceable only in simulations) lead to parallel cylinder morphologies; a behavior attributed to the entropic affinity of the minority block for the confining surface [39, 16]. While the basic nature of these interactions is understood, no theoretical perspective has been proposed that satisfactorily explains the experimental observations with regard to evaporation rate and surface effects.

Historically, Self-Consistent Field Theory has enjoyed great success as a predictive tool in block copolymer melt phase behavior due to the accuracy with which it models chain configura-

tional entropy and the general applicability of the Flory-Huggins model for the enthalpy of mixing unlike polymer segments. While equilibrium calculations give us insight into the local minima of the free energy surface and how the systems might respond to perturbations such as irregularities in wall profile, polydispersity, etc. they are somewhat limited in their ability to describe processing effects such as dynamic or non-equilibrium considerations. It is additionally important to recognize that if the details of how films are processed can impact their final structure, then the relevant ensemble to study is the one comprised of all *dynamical trajectories* that connect initial and final states - not just considerations of the film at equilibrium. Equilibrium calculations can give only information about a system that successfully samples all of configuration space, which a film undergoing evaporation and presumably the glass transition does not.

2.1.1 Morphology Control via Solvent Annealing

The subtle interplay between interactions with the surface and chain conformational entropy makes the processing windows for preferred structures narrow in many cases. This behavior has led to numerous experimental and theoretical studies of cylinder-forming copolymer thin films to try and develop a general strategy for annealing $C_\perp$. Towards this end, Hawker and Russell et al. made a significant contribution by introducing random copolymer brushes grafted to wafer substrates, creating a neutral mean-field environment for the copolymer blocks[19]. In fact, the majority of successful experiments resulting in perpendicular cylinders, with the exception of ultra-thin films, use this method. A few authors have also indicated that swelling films with solvent and rapidly drying them will promote perpendicular orientation of cylinder domains[28, 18, 27], and we note that the majority of experimental results were obtained using this method. Interestingly, Han et al. reported thermally annealed samples of thick films ($\sim$500nm or $\sim$14 d_0) which exhibited $C_\perp$, supporting the idea that truly neutral conditions promote perpendicular alignment as well, although these conditions require great care to achieve[14]. The stability of $C_\perp$ in these results may be partly explained by a recent study demonstrating that random copolymer brushes actually enhance the stability of $L_\perp$ over neutral, neat surfaces, a result we expect applies to cylinders as well[33]. A comprehensive understanding of micro-phase separation requires addressing a broad range of possible influences, but one of the most puzzling and difficult to test experimentally is the effect of solvent evaporation rate. No quality, controlled simulation or experimental studies have been performed with the time or length scales required to study the process from swollen to ordered, and we believe this represents a gap in the solvent annealing and thin film literature. The purpose of our program is to isolate and study the dynamical aspects of micro-phase separation during the film drying process. Key questions include whether evaporation rate as a controlled, independent variable can effect a change in micro-domain orientation, whether a concentration-dependent kinetic mobility is required to explain such an effect, and working out the consequences for controlling the morphology alignment in copolymer films of varying thicknesses.

2.2 Theoretical Framework

2.2.1 Polymer Model

In choosing a model to study copolymer micro-phase separation, we are not concerned with, nor terribly interested in, chemistry-specific details that would be built into a complex equation of state or interaction potential[1]. It therefore proves most convenient to employ the standard Flory-Huggins polymer fluid model with finite compressibility for an ensemble of interacting chains and segment-sized solvent particles. This document focuses on a solvated copolymer system so while the method is quite general, equations will be derived for this case.

Consider an $A-B$ diblock copolymer immersed in monatomic fluid solvent S, interacting through local contact potentials:

$$u_{ij}(\mathbf{r}_i - \mathbf{r}_j) = k_B T \delta(\mathbf{r}_i - \mathbf{r}_j) v_0 \chi_{ij}$$

This potential of mean force prescription suffices to describe meso-scale segregation behavior due to unfavorable contact interactions between unlike polymer or solvent segments. It is convenient to transition to a more coarse-grained view of space and introduce microscopic density fields:

$$\hat{\rho}_S(\mathbf{r}) = \sum_{j=1}^{n_S} \delta(\mathbf{r} - \mathbf{r}_j)$$

$$\hat{\rho}_K(\mathbf{r}) = \sum_{j=1}^{n_P} \int_0^N \delta(\mathbf{r} - \mathbf{r}_j(s)) \delta_{Ks} ds$$

Here K indicates block segment types (A or B) and δ_{Ks} simply filters to count only segments of type K in the integral. Notice also that the polymer chains are described by a space-curve $\mathbf{r}_j(s)$ which gives the location in space of the sth segment in the jth chain. With these definitions, the total interaction energy of the system can be described as a sum of pairwise interactions and bonded interactions describing the energetics of chain conformations:

$$\beta U[\mathbf{r}^{n_S}, \mathbf{r}_j(s)^{n_P}] = \frac{3}{2b^2} \sum_{j=0}^{n_P} \int_0^N \left| \frac{d\mathbf{r}_j(s)}{ds} \right|^2 ds + \sum_{K,K'} v_0 \chi_{KK'} \int \hat{\rho}_K(\mathbf{r}) \hat{\rho}_{K'}(\mathbf{r}) d\mathbf{r}$$
$$+ v_0 \frac{\zeta}{2} \int (\hat{\rho}_A + \hat{\rho}_B + \hat{\rho}_S + \rho_w - \rho_0)^2 d\mathbf{r}$$

An additional term proportional to ζ has been appended to enforce finite compressibility of the fluid through a Helfand harmonic penalty for deviating from the uniform density ρ_0. The field ρ_w is a place-holder for substrate and free surface profiles that will be used to model preferential surfaces.

[1] It is worth mentioning, however, that since the density dynamics scheme requires explicit reference to the density fields in the theory, a species model formulation of the field theory proves most convenient. With this commitment, requirements that our chosen interaction potential be positive-definite and invertible are relaxed, opening up the opportunity to study density dynamics in heterogeneous systems with more complicated interaction potentials

The canonical partition function for the system follows from standard statistical mechanics as an integral over all relevant degrees of freedom, summing the Boltzmann weight of each state [5]:

$$\mathcal{Z}_C(n_s, n_P, V, T) = \frac{1}{n_s! n_P! \lambda_T^{3(n_s+n_P N)}} \prod_{j=1}^{n_P} \int \mathcal{D}\mathbf{r}_j(s) \prod_{k=1}^{n_s} \int d\mathbf{r}_k \exp\left(-\beta U[\mathbf{r}^{n_S}, \mathbf{r}_j(s)^{n_P}]\right)$$

2.2.2 Field Theory Formulation

In the particle-based model, evaluation of the ensemble partition function requires integrating over all possible chain configurations and particle positions, calculating the N^2 potential energy contributions from all polymer segment and solvent molecule interactions. However, we can decouple inter-chain interactions by introducing continuous density and auxiliary potential fields through the Fourier representation of the delta functional, which constrains our continuous fields to agree with the particle formulation's microscopic densities at each point in space:

$$\delta[\hat{\rho} - \rho] = \int \mathcal{D}w \exp\left(i \int w(\mathbf{r}) \left(\rho(\mathbf{r}) - \hat{\rho}(\mathbf{r})\right)\right)$$

The partition function for the field theory becomes:

$$\mathcal{Z}_C(n_P, n_s, V, T) = \mathcal{Z}_0 \prod_i \int \mathcal{D}w_i \int \mathcal{D}\rho_i \ \exp(-\beta H[\{w_i\}, \{\rho_i\}]) \tag{2.1}$$

where $H[\{w_i\}, \{\rho_i\}]$ is given by:

$$\begin{aligned} H[\{w_i\}, \{\rho_i\}] = &\sum_{K,K'} v_0 \chi_{KK'} \int \rho_K(\mathbf{r}) \rho_{K'}(\mathbf{r}) d\mathbf{r} \\ &+ v_0 \frac{\zeta}{2} \int \left(\rho_A(\mathbf{r}) + \rho_B(\mathbf{r}) + \rho_S(\mathbf{r}) + \rho_w(\mathbf{r}) - \rho_0\right)^2 d\mathbf{r} \\ &- i \sum_K \int \rho_K(\mathbf{r}) w_K(\mathbf{r}) \, d\mathbf{r} - \sum_i n_i \log Q_i[\{w\}_i] \end{aligned} \tag{2.2}$$

The term proportional to $\log Q$ in the Hamiltonian represents the free energy of a single component (either isolated polymer chain or solvent particle) exposed to the external field(s) $\{w_i\}$ associated with that component. For example, a copolymer chain experiences two external potentials: w_A and w_B for interactions with each segment type. To compute this term, we turn to the chain propagator formalism described in [11], which provides a convenient platform for computing the single-chain partition function and related quantities, by deriving a Fokker-Planck equation from the transition probability rules that define the polymer chain model used. For the continuous Gaussian chain, the propagator satisfies:

$$\partial_s q(\mathbf{r}, s) = \frac{Nb^2}{6} \nabla^2 q(\mathbf{r}, s) - w(\mathbf{r}) q(\mathbf{r}, s) \tag{2.3}$$

$$q(\mathbf{r}, 0) = 1$$

Solutions represent the statistical weight of finding the end of a polymer chain of length 's' at position '**r**'. It can further be shown that the partition function can be written in terms of the chain propagator as:

$$Q[w] = \frac{1}{V}\int_V q(\mathbf{r},N)d\mathbf{r} \tag{2.4}$$

Given that Q represents a single-chain partition function acting within an effective chemical potential field, we can use the thermodynamic connection formula from statistical mechanics to write the expectation value of the segment density in terms of Q and therefore $q(\mathbf{r},s)$:

$$-n_P\frac{\delta \log Q}{\delta w(\mathbf{r})} = \tilde{\rho}(\mathbf{r};[w]) \tag{2.5}$$

From this we can derive the density operator from equation (2.5) in terms of single chain propagators:

$$\tilde{\rho}[w] = \frac{n_P}{VQ[w]}\int_0^N q(\mathbf{r},s)q^\dagger(\mathbf{r},N-s)ds \tag{2.6}$$

This density operator will enter into the evaluation of the thermodynamic force described in later sections.

2.2.3 Dynamics

The equations derived in the previous section suffice to study the equilibrium properties of a swollen polymer film. In order to study the dynamics of solvent evaporation, we turn to a dynamical extension of this theory wherein we track the dynamics of the slow, collective density field variables to which the auxiliary w fields are adiabatically slaved. The general procedure is to initialize the simulation in an equilibrium thin-film state, then begin to allow solvent to evaporate through the air/film interface (details to follow). This perturbation pushes the system out of equilibrium and we describe its response by the diffusive dynamics below. This method was first introduced by Fraaije and coworkers who posited a mean-field effective potential acting on a separate ensemble of ideal gas chains [9]. The minimization criterion used to determine this mean-field potential yields an equivalent expression as the partial saddle-point approximation to the Self-Consistent Field Theory employed in this work.

Modeling Evaporation

As indicated previously, we find it convenient to confine our density fields between explicit substrate and free surface phases (see illustration in Figure 2.1). These additional fields simply enforce an interfacial profile and allow for preferential surfaces to be simulated by choosing suitable surface/substrate interactions. In addition, the free surface profile provides an extended region into which solvent may diffuse and be removed from the simulation continuously, modeling evaporation. This reproduces the essential aspects of evaporation, while giving us the freedom we need to specify boundary conditions independent of our choice for evaporation rate. This proves to be

essential as boundary conditions on the chain propagators in the Self-Consistent Field Theory must produce density operators with boundary conditions consistent with those imposed on the dynamical density fields. The evaporation model we use is a simple bimolecular reaction mechanism:

$$-r_S(\mathbf{r}) = k\rho_S(\mathbf{r})\rho_w(\mathbf{r})$$

where solvent is continuously removed from regions of large overlap between solvent and surface mask. Here the function $r_S(\mathbf{r})$ is the rate of solvent removal, which is space-dependent only to concentrate removal near the free surface. Its integral over z is the evaporative flux; instead of distributing this loss over a delta function interface, we smear it out over the region of overlap between the solvent density field and the "air/vapor phase" wall mask. The volume change due to evaporation is therefore given by

$$\frac{dV}{dt} = \int (-r_S(\mathbf{r}))d\mathbf{r}$$

Since evaporation occurs only through the top surface, we can reduce this to an equation of motion for the film thickness $L_z(t)$:

$$\frac{dL_z}{dt} = \frac{1}{L_x L_y}\int k\rho_S(\mathbf{r})\rho_w(\mathbf{r})d\mathbf{r}$$

This evaporation model allows us the convenient choice of Neumann boundary conditions, which are simple to apply both to the dynamics and chain propagator equations with consistent results. Some intuition for how the reaction rate constant translates into the rate of film de-swelling (and, therefore, evaporation) may be gleaned from Figure 2.2, which shows the film thickness as a function of simulation time under the range of reaction rates used in this study.

Concentration Dynamics Equations

Polymer concentration dynamics are often written in the form [17, 24]:

$$\partial_t \rho_i(\mathbf{r},t) = -\sum_j \int dr' M_{ij}(\mathbf{r},\mathbf{r}')\frac{\delta\mathcal{F}}{\delta\rho_j(\mathbf{r}')} + \eta(\mathbf{r},t) \tag{2.7}$$

where M_{ij} is the mobility matrix, written as a convolution with the non-local nature of polymer kinetics in mind. Formally, the matrix is given by:

$$M_{ij}(\mathbf{r},\mathbf{r}') = n\left\langle \frac{\partial\hat{\rho}_i(\mathbf{r})}{\partial\mathbf{r}_j(s)}\cdot\hat{M}\cdot\frac{\partial\hat{\rho}_j(\mathbf{r}')}{\partial\mathbf{r}_j(s)}\right\rangle$$

where the average is taken over all possible chain conformations. A common approximation is to take $\hat{M}$ to be the identity matrix scaled by an effective diffusivity. This is known as the local coupling approximation and leads to the following equations of motion [24]:

$$\partial_t \rho_i(\mathbf{r},t) = \nabla\cdot\rho_i(\mathbf{r},t)\sum_j \Lambda_{ij}\nabla\frac{\delta\mathcal{F}}{\delta\rho_j} \tag{2.8}$$

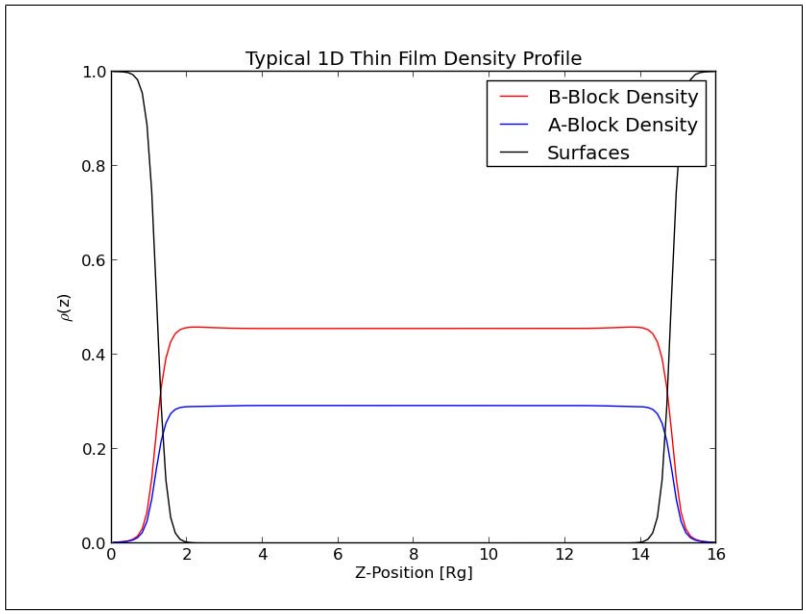

Figure 2.1. Typical profile of equilibrated thin film. Copolymer densities shown along with confining substrate/surface profiles. In this example f=0.4, χN_{AB}=10 and ζN = 1000.

Including the reaction terms we have:

$$\partial_t \rho_i(\mathbf{r},t) = \nabla \cdot \rho_i(\mathbf{r},t) \sum_j \Lambda_{ij} \nabla \frac{\delta \mathcal{F}}{\delta \rho_j} + k_i \rho_i \rho_w$$

As solvent leaves the system, the domain will shrink to accommodate the lost volume. This could be accounted for by solving the equations on a variable grid domain, but a more elegant approach is to scale out the domain size[2] $\bar{z} = \frac{z}{L(t)}$, leading to:

$$\begin{aligned} \partial_t \rho(\bar{\mathbf{r}},t) &= \partial_z \rho(\mathbf{r},t)\, \partial_t z(t) + \partial_t \rho(\mathbf{r},t) \\ &= \frac{zV'}{V(t)} \partial_{\bar{z}} \rho(\bar{\mathbf{r}},t) + \frac{1}{V(t)^2} \nabla \cdot \rho_i(\bar{\mathbf{r}},t) \sum_j \Lambda_{ij} \nabla \frac{\delta \mathcal{F}}{\delta \rho_j(\bar{\mathbf{r}})} + k_i \rho_i(\bar{\mathbf{r}},t) \rho_w(\bar{\mathbf{r}}) \end{aligned} \tag{2.9}$$

We are finally left with a generalized diffusion equation augmented with the transport term we get from scaling out our time-dependent domain size. The only factor that must still be explained is the thermodynamic force driving our dynamics $\frac{\delta \mathcal{F}}{\delta \rho}$.

[2]Notice we have tacitly assumed here that grid spacing, and hence compression of the film, occurs linearly over the domain by our choice of map $z \to \bar{z}$. Different choices for how the grid changes with time (i.e. $z(t)$) will result in different forms of the transport term.

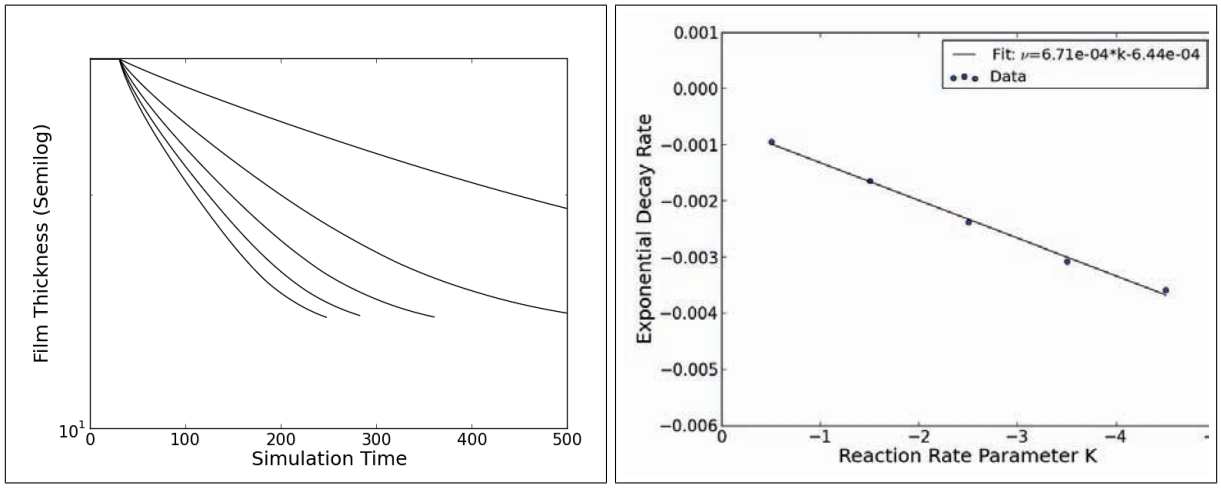

Figure 2.2. Left: Film thickness as a function of simulation time (semi-log) for various evaporation rates k=-1 (top), -2, -3, -4, and -5 (bottom). The behavior at intermediate times is observed to be approximately exponential. Right: A linear fit to this region yields an exponential decay rate which is plotted vs the reaction rate parameter k. The film deswelling rate is then found to be related to the reaction rate parameter k as $L(t;k) \approx L_0 \exp(.0007k)$.

Evaluating the Thermodynamic Force

Recalling the standard thermodynamic connection formula along with our field theory partition function:

$$\beta A = \quad \log \mathcal{Z} = A_0 \quad \log\left(\prod_i \int \mathcal{D}w_i \int \mathcal{D}\rho_i \ \exp(\quad \beta H[\{w_i\},\{\rho_i\}])\right)$$

Now the purpose of this analysis is to isolate the free energy of a given density configuration so that the thermodynamic force may be resolved as the first variation with respect to perturbations in this imposed density field. The reduced partition function under this constraint may be written:

$$\beta A[\{\rho_i\}] = A_0 \quad \log\left(\prod_i \int \mathcal{D}w_i \ \exp(\quad \beta H[\{w_i\},\{\rho_i\}])\right)$$

Employing the saddle-point approximation, we can take the density free energy functional to be simply the mean-field Hamiltonian:

$$\beta A[\{\rho_i\}] = A_0 + \beta H[\{\rho_i\},\{w_i^*\}]$$

Taking the functional derivative with respect to the density field ρ_j we obtain an effective chemical potential field experienced by component j:

$$\beta\mu_j = \frac{\delta\beta A[\{\rho_i\}]}{\delta\rho_j} \approx \left.\frac{\beta H[\{\rho_i\},\{w_i\}]}{\delta\rho_j}\right|_{\{w_i^*\}} \tag{2.10}$$

Here, the Hamiltonian and its derivatives are evaluated at a set of fields $\{w_i^*\}$ which satisfy the following set of optimization conditions:

$$\left.\frac{\delta H[\{w_i\},\{\rho_i\}]}{\delta w_j}\right|_{w_j^*} = -n \left.\frac{\delta \log Q}{\delta w_j}\right|_{w_j^*} - \rho_j = 0 \tag{2.11}$$

The first term in this equation is the density operator described previously. This condition, therefore, implies that the external fields we seek are those for which the equilibrium density distribution under the influence of these external fields matches the current dynamical densities. A more physically intuitive way of thinking about this is that the internal stresses in the polymer fluid are indicated by the forces one must impose on the system in order to make the current density distribution the equilibrium one.

2.2.4 Summary of Equations for the Current System

In this work we focus on an AB diblock copolymer mixed with a small molecule, monatomic fluid solvent. While the nature of the external potential for polymer species is complex and non-local, there is a closed form solution for the solvent species owing to its simple configuration integral. The density operator for a monatomic fluid is given by the following expression:

$$\tilde{\rho_S}(\mathbf{r};w_S) = \frac{n_S}{VQ[w_S]}\exp\left(-w_S\right)$$

We always have the freedom to choose Q when searching for the auxiliary potentials, since the volume average value of w does not impact the density operator - it simply increases the normalization factor (Q), so we take Q[w]=1.0 for simplicity. Therefore, we can invert this expression directly to solve for w_S:

$$w_S = -\log\left(\frac{V\tilde{\rho}_S(\mathbf{r};w_S)}{n_S}\right)$$

Plugging this expression in for w_S in the solvent flux equation, evaluating the functional derivative with (2.2), and recognizing that the optimization condition mentioned above implies $\tilde{\rho}_S(\mathbf{r};w_S) = \rho_S(\mathbf{r},t)$, we get:

$$\begin{aligned}
J_S(\mathbf{r},t) &= -\rho_S(\mathbf{r},t)\Lambda_{SS}\nabla\frac{\delta H}{\delta\rho_S(\mathbf{r},t)} \\
&= -\rho_S(\mathbf{r},t)\Lambda_{SS}\left(\sum_j \chi_{Sj}\nabla\rho_j(\mathbf{r},t) + \zeta\left(\sum_j \nabla\rho_j(\mathbf{r},t)\right) + \nabla\log\left(\frac{V\rho_S(\mathbf{r},t)}{n_S}\right)\right) \\
&= -\rho_S(\mathbf{r},t)\Lambda_{SS}\left(\sum_j \chi_{Sj}\nabla\rho_j(\mathbf{r},t) + \zeta\left(\sum_j \nabla\rho_j(\mathbf{r},t)\right) + \frac{\nabla\rho_S(\mathbf{r},t)}{\rho_S(\mathbf{r},t)}\right)
\end{aligned}$$

Here it is clear that the factor of density in our kinetic mobility acts to cancel the $\frac{1}{\rho_S}$ term from taking a derivative of the log, leading to the Fick's law behavior we expect for the solvent diffusion. Plugging this result into the continuity equation, including the transport term and reduced

dimensions, we get our solvent concentration dynamics:

$$\begin{aligned}\partial_t \rho_S(\bar{\mathbf{r}},t) &= -\nabla\cdot J_S(\bar{\mathbf{r}},t) + \frac{zV'}{V(t)}\partial_{\bar{z}}\rho_S(\bar{\mathbf{r}},t) + k\rho_S(\bar{\mathbf{r}},t)\rho_w(\bar{\mathbf{r}}) \\ &= \frac{1}{V(t)^2}\left(\nabla\cdot\rho_S(\bar{\mathbf{r}},t)\Lambda_{SS}\left(\sum_j \chi_{Sj}\nabla\rho_j(\bar{\mathbf{r}},t) + \zeta\left(\sum_j \nabla\rho_j(\bar{\mathbf{r}},t)\right)\right) + \nabla^2\rho_S(\bar{\mathbf{r}},t)\right) \\ &+ \frac{zV'}{V(t)}\partial_{\bar{z}}\rho_S(\bar{\mathbf{r}},t) + k\rho_S(\bar{\mathbf{r}},t)\rho_w(\bar{\mathbf{r}})\end{aligned} \tag{2.12}$$

The polymer equations follow more directly from (2.9) as:

$$\begin{aligned}\partial_t \rho_A(\bar{\mathbf{r}},t) &= \frac{1}{V(t)^2}\left(\nabla\cdot\rho_A(\bar{\mathbf{r}},t)\Lambda_{AA}\left(\sum_j \chi_{Aj}\nabla\rho_j(\bar{\mathbf{r}},t) + \zeta\left(\sum_j \nabla\rho_j(\bar{\mathbf{r}},t)\right)\right) - \nabla w_A(\bar{\mathbf{r}},t)\right) \\ &+ \frac{zV'}{V(t)}\partial_{\bar{z}}\rho_A(\bar{\mathbf{r}},t)\end{aligned} \tag{2.13}$$

$$\begin{aligned}\partial_t \rho_B(\bar{\mathbf{r}},t) &= \frac{1}{V(t)^2}\left(\nabla\cdot\rho_B(\bar{\mathbf{r}},t)\Lambda_{BB}\left(\sum_j \chi_{Bj}\nabla\rho_j(\bar{\mathbf{r}},t) + \zeta\left(\sum_j \nabla\rho_j(\bar{\mathbf{r}},t)\right)\right) - \nabla w_B(\bar{\mathbf{r}},t)\right) \\ &+ \frac{zV'}{V(t)}\partial_{\bar{z}}\rho_B(\bar{\mathbf{r}},t)\end{aligned} \tag{2.14}$$

2.3 Numerical Solution

2.3.1 Discretized Dynamics Equations

We follow the method described in [3] and develop a semi-implicit scheme to integrate our equations of motion with a variable (density-dependent) mobility[3]. Notice that the form of our flux corresponds to Fick's law so that monatomic fluid solvents will have *no w-field contribution*. Instead, a term $\nabla^2\rho$ is added to solvent-species equations. Starting from a discretized form of equation (2.9):

$$\begin{aligned}\rho_i^{t+1} &= \rho_i^t + \Delta t\sum_j\left(\frac{1}{V^t}\right)^2\nabla\cdot\rho_i^t\Lambda_{\mathrm{ij}}\nabla\mu_j + \mathbf{S}_{\mathrm{ij}}\left(\frac{1}{V^{t+1}}\right)^2\nabla^2\rho_j^{t+1} \\ &+\Delta t\ \frac{zV'}{V^t}\partial_{\bar{z}}\rho_i^t \\ &+\Delta t\ k_{\mathrm{i}}\ \rho_i^t\ \rho_w\end{aligned}$$

[3]To avoid confusion regarding the mixture of direct and inner products in the equations, I have opted to index the components explicitly using summation notation. Indices therefore run over all components in the theory (typically 3: Copolymer blocks A and B, and solvent S)

where

$$\begin{aligned}
\mu_j &= \frac{\delta H}{\delta \rho_j} \\
\mathbf{S}_{ij} &= 0 \qquad i \neq j \\
&= 1 \qquad i = j \text{ and } i \text{ is a solvent type}
\end{aligned}$$

Spatial derivatives are left in operator form since they will be solved in reciprocal space using the appropriate Fourier transforms for the imposed boundary conditions. The chemical potential field includes the auxiliary potentials w_i which, for polymer species, is non-linear in the density fields. However, by expanding the fields in a perturbation from a homogeneous state to first order in the density we can extract the portion of the chemical potential field contribution which is linear in the density. Adding and subtracting this term at the future and present times respectively treats the linear part of the thermodynamic force implicitly and dramatically enhances numerical stability. This weak-inhomogeneity expansion procedure is described in reference [11] and results in the following semi-implicit scheme[4]:

$$\begin{aligned}
\rho_i^{t+1} = \rho_i^t &+ \Delta t \sum_j \left(\frac{1}{V^t}\right)^2 \nabla \cdot \rho_i^t \Lambda_{\mathrm{ij}} \nabla \mu_j + S_{\mathrm{ij}} \left(\frac{1}{V^{t+1}}\right)^2 \nabla^2 \rho_j^{t+1} \\
&+ \Delta t \frac{\max(\rho_i)}{2} \sum_j \Lambda_{\mathrm{ij}} \nabla^2 \left(\left(\frac{1}{V^{t+1}}\right)^2 (\mu_{\mathbf{lin}})_{ij}^{t+1} * \rho_j^{t+1} - \left(\frac{1}{V^t}\right)^2 (\mu_{\mathbf{lin}})_{ij}^{t} * \rho_j^{t} \right) \\
&+ \Delta t \ \frac{zV'}{V^t} \partial_{\bar{z}} \rho_i^t \\
&+ \Delta t \ k_{\mathrm{i}} \ \rho_i^t \ \rho_w
\end{aligned} \tag{2.15}$$

The form that W_{lin} takes is a convolution with the density field, indicated by '$*$' above. This will become a multiplication when solved in Fourier space. Fourier-space representations will be indicated by $\hat{f}$. The matrices above are defined as:

$$\begin{aligned}
\mu_i &= \sum_j \left(\chi_{ij} + \zeta_{ij}\right) \rho_j - \zeta \rho_0 - w_j \\
(\mu_{\mathbf{lin}})_{ij} &= \chi_{ij} + \zeta_{ij} - (\mathbf{W}_{\mathbf{lin}})_{ij} \\
\widehat{W}_{lin} &= \left(\begin{array}{c|cc}
-\dfrac{\hat{\mathbf{g}}_{BCP}^{-1}}{N\phi_{BCP}} & \multicolumn{2}{c}{0} \\
\hline
0 & -\dfrac{1}{\alpha N \phi_{HP} \hat{g}} & 0 \\
 & 0 & -\dfrac{1}{\phi_{Solv}}
\end{array}\right), \hat{\mathbf{g}}_{BCP} = \begin{pmatrix} \hat{g}_A & \hat{g}_{AB} \\ \hat{g}_{AB} & \hat{g}_B \end{pmatrix}
\end{aligned}$$

[4]The reference treats the weak inhomogeneity expansion for a homopolymer. However, the extension to block copolymers is somewhat trivial and has therefore been omitted for brevity. The only additional consideration is in performing the integral over contour position s, since the w-fields are now s-dependent. This leads to the introduction of cross-terms which appear as the off-diagonal elements in the $\left(\widehat{W}_{lin}\right)_{00}$ block matrix above.

The $\widehat{W}_{lin}$ matrix is given as an example for a block copolymer, homopolymer, monatomic fluid system. The system considered in this work, however, includes no homopolymer component and our choice of mobility leads us to neglect the linear part of the solvent field (neglect, in fact, the w field altogether). The $\hat{g}$ functions indicated above are the Fourier transforms of the Debye scattering functions for block copolymers defined by[4]:

$$\hat{g}_A(\mathbf{k}) = \tfrac{2}{\mathbf{k}^4}\left(f\mathbf{k}^2 + \exp\left(-\mathbf{k}^2 f\right) - 1.0\right) \tag{2.16}$$

$$\hat{g}_B(\mathbf{k}) = \tfrac{2}{\mathbf{k}^4}\left((1.0-f)\mathbf{k}^2 + \exp\left(-\mathbf{k}^2(1.0-f)\right) - 1.0\right) \tag{2.17}$$

$$\hat{g}_{AB}(\mathbf{k}) = \tfrac{1}{\mathbf{k}^4}\left(1.0 - \exp\left(-\mathbf{k}^2 f\right)\right)\left(1.0 - \exp\left(-\mathbf{k}^2(1.0-f)\right)\right) \tag{2.18}$$

Numerical Solution

These equations are solved in a straight-forward way, first securing forms of each equation that are local in k-space and then updating each mode individually. Expanding each side of (2.15) in a Fourier series (cosine series in z):

$$\begin{aligned}
\widehat{\rho}_i^{t+1} = \widehat{\rho}_i^t &+ \Delta t \sum_j \left(\frac{1}{V^t}\right)^2 \nabla\cdot\widehat{\rho_i^t \Lambda_{\mathrm{ij}} \nabla \mu_j} - S_{\mathrm{ij}}\left(\frac{1}{V^{t+1}}\right)^2 k^2 \widehat{\rho}_j^{t+1} \\
&-\Delta t \frac{\max(\rho_i)}{2}\sum_j \Lambda_{\mathrm{ij}} k^2 \left(\left(\frac{1}{V^{t+1}}\right)^2 (\widehat{\mu_{\mathrm{lin}}})_{ij}^{t+1}\,\widehat{\rho}_j^{t+1} - \left(\frac{1}{V^t}\right)^2 (\widehat{\mu_{\mathrm{lin}}})_{ij}^{t}\,\widehat{\rho}_j^{t}\right) \\
&+\Delta t\ \widehat{\frac{zV'}{V^t}\partial_{\bar{z}}\rho_i^t} \\
&+\Delta t\ k_{\mathrm{i}}\ \widehat{\rho_i^t\ \rho_w}
\end{aligned}$$

The equation of motion for volume discretizes simply with a forward Euler method in time:

$$V^{t+1} = V^t + \Delta t \sum_j \int k_j \rho_j^t \rho_w$$

Notice we now have a set of n equations (where n is the number of density fields), each local in k but coupled amongst each other by interaction terms. We can therefore solve these equations by solving the nxn system for each Fourier mode $\mathbf{k}$:

$$\begin{aligned}
\widehat{\rho}_i^{t+1} = &\sum_{jk}\left(\mathbf{A}^{-1}\right)_{ik}\mathbf{B}_{kj}\widehat{\rho}_j^{\,t} \\
&+\Delta t \sum_{jk}\left(\mathbf{A}^{-1}\right)_{ij}\left(\frac{1}{V^t}\right)^2 \nabla\cdot\widehat{\rho_j^t \Lambda_{\mathrm{jk}} \nabla \mu_k} \\
&+\widehat{\frac{zV'}{V^t}\partial_{\bar{z}}\rho_j^t} \\
&+k_{\mathrm{j}}\ \widehat{\rho_j^t\ \rho_w}
\end{aligned} \tag{2.19}$$

where

$$\mathbf{A} = \left(\mathbf{I} + \Delta t\ k^2 \left(\frac{1}{V^{t+1}} \right)^2 \Lambda \cdot \left(\mathbf{S} + \frac{\max(\rho)}{2} \mu_{\mathbf{lin}}^{t+1} \right) \right)$$

$$\mathbf{B} = \left(\mathbf{I} + \Delta t\ k^2 \frac{\max(\rho)}{2} \left(\frac{1}{V^t} \right)^2 \Lambda \cdot \mu_{\mathbf{lin}}^{t} \right)$$

Our solution procedure is now complete, provided we can compute the spatially varying thermodynamic potentials μ_i. Following from equation (2.11), we employ the following steepest descent pseudo-dynamics to the w fields. This equation of motion is integrated in "time" until a stationary point converges:

$$\frac{dw_j}{dt} = \frac{\delta H}{\delta w_j} = \tilde{\rho}_j[w_j] - \rho_j \tag{2.20}$$

Equation (2.19) is written essentially how it is solved in actual implementation, although the linear algebra is performed using an open source library (Eigen). First, the explicit vectors are evaluated by spectral evaluation of the gradient, subsequent real-space multiplication, divergence operation, and finally a Discrete Fourier Transform to solve for the Fourier coefficients. Similarly, the reaction and transport fields are computed. Then, for each k-mode, the A^{-1} and B matrices are computed, the right hand side evaluated, and the density fields are updated.

2.3.2 Simulation Details

In this section, details concerning the setup and execution of the density dynamics simulations will be described, along with an illustration of the method and typical features. By including these illustrations, I simply hope to communicate the tendencies and quirks that exist in our model that wouldn't be appropriate to include in the results.

Size Considerations: Polymers and Point Particles

One feature worth discussing is the fact that the coarse-grained nature of our model makes incorporating realistic separations of scale difficult. There is an inherent length scale associated with the copolymers that is absent in the physics of monatomic fluids in the theory. Fully appreciating the difference in effective volume of the two species would require a more physical treatment of the air/film and substrate/film interfaces and lead to unnecessarily expensive simulations. This is entirely a consequence of simulating large systems which have, in the physical system, extremely sharp features (at the film/air interface) all in a continuum, mesoscale description. This isn't an issue, however, so long as we respect the limitations it places on the parameters we can realistically use. Practically speaking, this problem occurs when trying to confine the film between two masks. If the interactions with the surface are taken to be small, both density fields will naturally flow into the masked region, violating incompressibility. The harmonic pressure penalty acts equally on both the solvent and polymer, so the two responses differ only by the additional translational

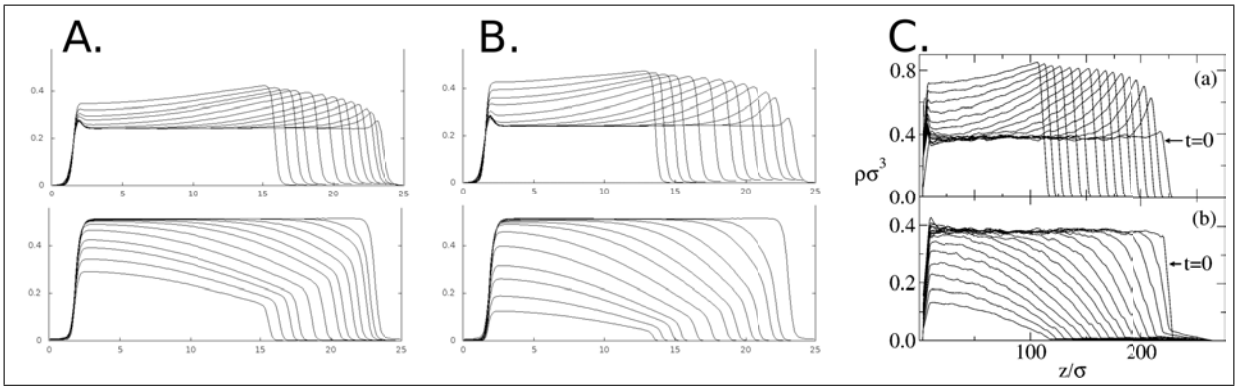

Figure 2.3. Typical polymer (top) and solvent (bottom) density profiles over the course of a simulation at standard, neutral conditions: $\chi N_{ASub} = \chi N_{BSub} = \chi N_{ASurf} = \chi N_{BSurf} = 1.0$, $\chi N_{SSurf} = \chi N_{SSub} = 3.0$ and k=-1.0 (A) and k=-7.0 (B). Profiles may be compared with the molecular dynamics result in reference [34] (C).

entropy lost due to confinement. For the large polymer, this entropy effect is damped by a $\frac{1}{N}$ scaling. For this reason, the polymer component density is driven near zero, while the solvent density remains finite (typically $\sim 10^{-1}$). We are then left with a continuum polymer density that feels a persistent enthalpic pressure to vacate regions of space where its volume fraction is $\sim 10^{-3}$. Practical experience shows that any but the most microscopic time steps will lead to driving this density negative during the simulation with disastrous consequences. For this reason, our copolymers are taken to be larger than the solvent species by only a factor of $\sim$10 (N_{BCP}=10). This choice leads to manageable wall interactions while including the difference in translational entropy of the two components in the model.

Choosing Thin Film Parameters

Counting every degree of freedom available to the simulation would yield an unwieldy number of searchable axes, which would simply serve to obscure the physically relevant parameters. For this reason, a number of judicious choices were made with regard to base-line surface and substrate interactions ($\chi N_{ASub}, \chi N_{BSub}, \chi N_{SSub}, \chi N_{ASurf}, \chi N_{BSurf}$, and χN_{SSurf}), copolymer size N_{BCP}, and substrate/free surface wall profiles. These choices were made for computational convenience and to reproduce the expected density profiles during evaporation as observed in molecular dynamics simulations by Grest and coworkers[34] which track the average 1D polymer and solvent density profiles during evaporation (Figure 2.3). Since our dynamics is essentially a density functional theory, we are concerned with reproducing reasonable density fields in the region of interest (the bulk) while remaining somewhat agnostic about the behavior in the masked regions. The gradients in solvent concentration over the z-domain, for example, is a feature of the dynamics that must be resolved appropriately while the decay of solvent into the masked region is entirely insignificant.

2.4 Results

2.4.1 Evaporation-Induced Ordering Fronts: Symmetric Copolymer Case

In block copolymer thin films, introducing a vapor phase with good solvents for both blocks will result in the diffusion of solvent into the material. Since the interaction potential is described by a local contact potential which is proportional to the local segment density, the effective ordering strength is reduced by simple dilution of the polymer concentration in the film, suppressing micro-phase separation. Upon exposing the film to a dry environment, solvent will begin to leave through the exposed surfaces, setting up concentration gradients of solvent (and therefore effective segregation strength) within the film. The first region of the material to micro-phase separate will therefore be the uppermost region of the film and the order will subsequently propagate into the film from the surface.

Non-Local Effects Due to Bonded Interactions

The thermodynamic potential that governs micro-phase separation in our model accounts for block connectivity through the chain propagator formalism, leading to a coupling between the ordering of one block and the subsequent ordering of the connected block. This behavior sets up a decaying wave of density correlations from ordered regions into neighboring disordered regions. This is to be contrasted from phase separation in simple fluids where there is generally no strong coupling between the phases (hydrodynamic effects neglected) and phase separation can occur with a clean, sharp interface between ordered and disordered regions. This may prove to have significant consequences for the dynamics of micro-phase separation in block copolymer materials.

When an ordered phase develops at the free surface of a thin film, this seed can be thought of as a chemical pattern near the surface that the fluid below "sees" and responds to. As a result of this observation, the current prevailing wisdom suggests the following strategy: nucleate an ordering front with the preferred orientation and this will grow as a single grain into the film, leading to perfect structures following the seeded template. Figure 2.4 is a representative 2D result which demonstrates how non-local effects complicate the notion of a clean ordering front propagating into the bulk as a single grain. Instead, we observe periodic half-period shifts in the morphology which lead to bi-continuous structures in 3D simulations (not shown). We can begin to understand this phenomenon by thinking about the behavior of the nominally disordered fluid in the region just below the ordering front.

When an ordered lamellar morphology develops and impinges on a disordered region, the stripes have to terminate and join the bulk fluid. Typically we think of lamellae as made up of stretched polymer coils oriented perpendicular to the direction of the stripe, but in the terminal end-caps there will be dangling chains that now extend *along* the stripe. This is illustrated in figure 2.5, implying a chemical pattern directly below the ordering front that is actually the inverse of the lamellar pattern since it is comprised of the non-partitioned block. Hence, a slight checkerboard pattern is formed as a small layer beneath the ordering front. Notice also that there are two options

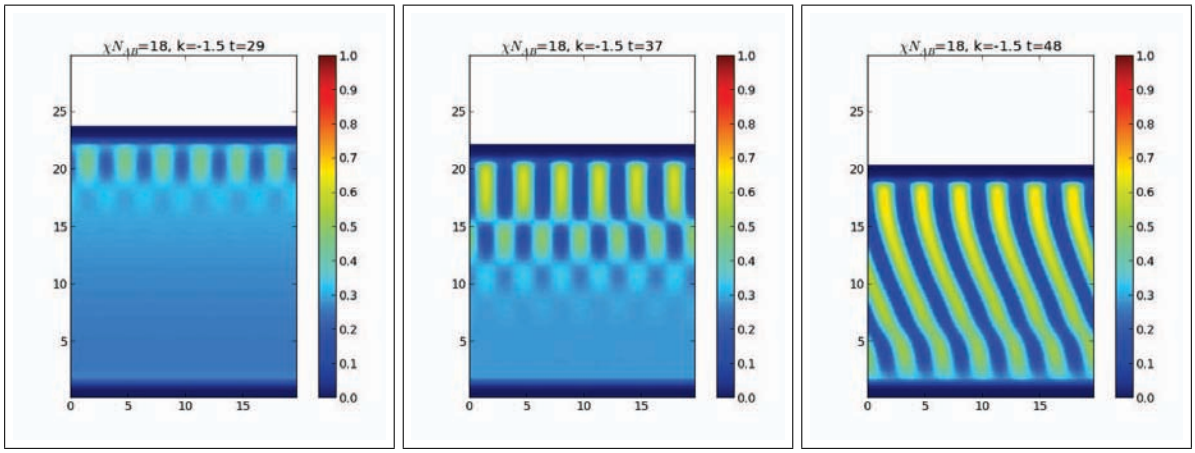

Figure 2.4. Typical ordering front in a symmetric (f=0.5) block copolymer thin film initially swollen with $\overline{\phi}_S(0)=\frac{1}{V(0)}\int \rho_S(\mathbf{r},0)d\mathbf{r}=0.6$, which corresponds to a disordered state. Strength of AB interactions and evaporation rate constant are provided in the titles of each subfigure. An $L_\perp$ front is seen to form near the free surface and extend into the film. Periodically, a splitting event is observed which is tentatively attributed to the non-local nature of the thermodynamic forces, discussed in the text.

for the growth of the morphology as this pattern develops, indicated by the left and right arrows in the figure. The left arrow implies shifting the capping chains up in a zipper-like motion to extend the lamellae, allowing additional chains to insert and re-form the cap. The right arrow shows the splitting phenomenon whereby the "linear response" chains simple stretch slightly to either side and form a new ordering front with a half-period shift. This new front now has the same properties as the old and is again susceptible to splitting. In simulations, we observe both of these occurring simultaneously (the ordering front continues to grow while splitting occurs).

In order to separate potential non-equilibrium effects from the equilibrium behavior, additional simulations were performed that directly imposed an interface between ordered and disordered fluid by enforcing a static neutral solvent density profile to occupy half of the box in the z-direction. The top film region is seeded with a lamellar morphology and the saddle-point solution is converged to determine the mean-field response of the disordered region near the interface. The results are shown in figure 2.6. Although not mentioned explicitly in the text, this phenomenon can also be observed in results by Muthukumar and coworkers [26]. In this paper, a chemical mask was imposed at one surface and the width of the pre-pattern was varied from commensurate with the periodicity of bulk lamellae to strongly stretched. This chemical pattern behaves exactly as our ordering front and sets up the same sort of checkerboard layer just beneath the pattern. The authors dismissed the effect as a consequence of unrealistic SCFT kinetics, but our diffusive dynamics scheme consistently produces these paths so the effect is observed both as a stable saddle-point in the mean-field approximation and as a probably kinetic event.

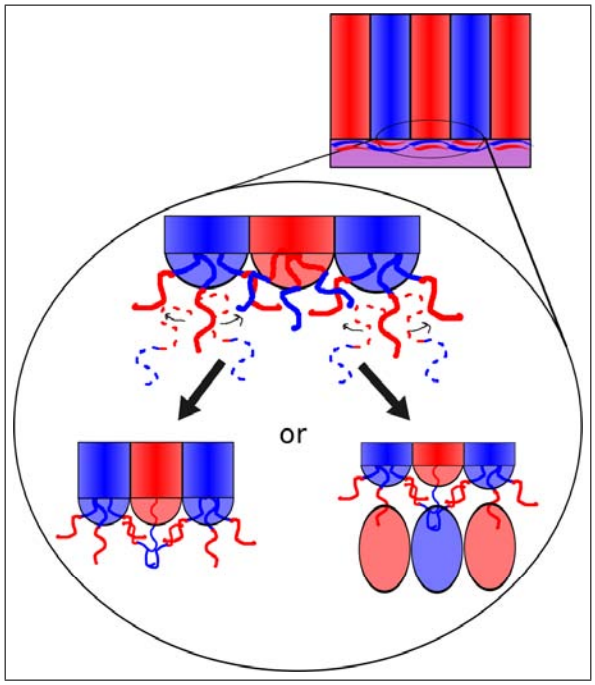

Figure 2.5. Illustration of how the copolymer fluid orders at the interface between an $L_\perp$ front and the disordered bulk film. The inset zooms in on this region, where the linear fluid response is indicated by dashed chains which orient to match the tails protruding from the caps of the lamellae. Essentially, blue stripes have red tails, attracting red tails from the disordered fluid, resulting in slight enrichment of blue tails just below that. Neighboring stripes exhibit analogous, inverted behavior (red-blue-red) which sets up a checker board layer below the ordering front.

2.4.2 Evaporation-Induced Ordering Fronts: Asymmetric Copolymer Case

Previous studies have elucidated a subtle effect of hard walls on the thermodynamics of copolymer melts due to bias in chain conformation statistics induced by the presence of an impermeable wall. It has been demonstrated, for example by Monte Carlo simulation [39], that the end-to-end distribution function in the direction perpendicular to the wall is compressed, implying that the chains tend to flatten along the wall which, for symmetric copolymers, leads to a very slight entropic preference for forming perpendicular lamellae. All dynamical simulations of ordering in symmetric copolymer systems we have performed corroborate this result: perpendicular lamellae spontaneously form near hard walls. The story is quite different for asymmetric copolymers, however. The broken symmetry leads to a slight entropic surface preference for the minority block. Interactions between A and B segments then tend to exclude the majority mid-segments from the surface region. This makes identifying neutral surface conditions extremely difficult, as the surfaces are no longer neutral when there are no enthalpic interactions between polymer segments

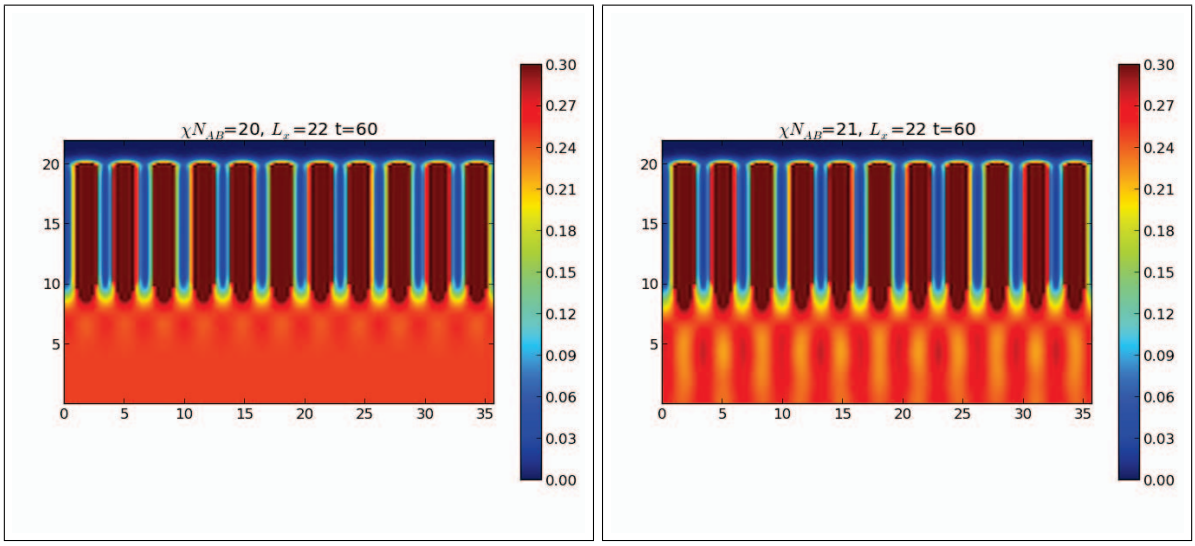

Figure 2.6. Saddle-point solutions converged using standard Self-Consistent Field Theory methods. The disordered region in the bottom half of the cell is maintained by masking the bottom region to maintain the total polymer density $\rho_A(z < 10) + \rho_B(z < 10)$=0.5 while $\rho_A(z \geq 10) + \rho_B(z \geq 10)$=1.0. In the dilution approximation, this leaves χN_{eff}=10 (left) and χN_{eff}=10.5 (right). At the ODT, the half-period shifted region is seen to extend to the rest of the cell, while below the ODT (left) the checkerboard pattern is observed in the viscinity ~2Rg of the interface.

and the wall. Instead, the surfaces are minority-block preferential unless exactly cancelled by an imposed surface field that neutralizes this effect. Since the nature of this preferential behavior is non-local, there is no guarantee that a local χ parameter is sufficient to exactly cancel the effect. Instead, a linear combination of solvent selectivity and surface contact interactions is used.

Sweeping for Neutral Surface Conditions

Ultimately, it is essential to identify conditions that effectively neutralize the free surface for cylinder-forming copolymer systems. Broad parameter sweeps are simply untenable due to computational complexity in 3D, and there is no direct analogue in 2D to the problem. However, notice the entire problem is introduced by asymmetry in the block fraction, not anything specific to the cylindrical morphology itself. I have therefore studied what I believe to be the analogous problem of aligning lamellae in slightly asymmetric copolymer systems perpendicular to the plane of the substrate. The slight asymmetry (f=0.45 in this study) does, in practice, lead to a parallel morphology for enthalpically neutral surfaces. In searching for neutral conditions, the solvent selectivity $\Delta\chi N_S = \chi N_{AS} \quad \chi N_{BS}$ and surface interactions χN_{ASurf} were varied from neutral to strongly minority block selective in solvent and majority block selective in surface. In order to quantify the

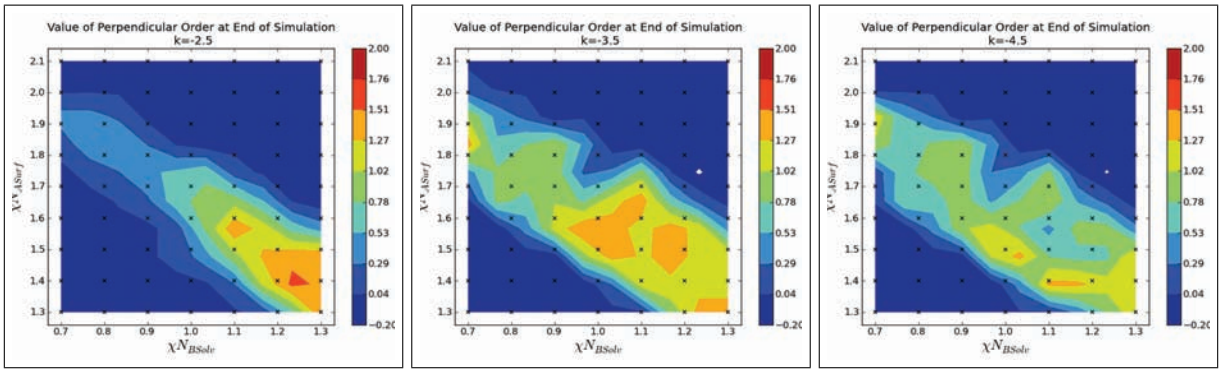

Figure 2.7. Heat maps showing the value of a perpendicular order parameter at the end of each simulation (when the remaining solvent fraction was less than 0.05). Perpendicular order is given as the sum of any contributing modes in the Fourier transform of the final morphology with $k_x \neq 0$ where x denotes the axis running parallel to the substrate, ie. $\psi = \sum_{k_x \neq 0} \widehat{\rho}(\mathbf{k})$. Notice that the region of perpendicular order grows between k=-2.5 and k=-3.5, but shows no further improvement with increasing evaporation rate. The surface disappears completely for evaporation rates below k=-2.0, indicating a minimum required evaporation rate to initiate a perpendicular ordering front.

result to map on a phase diagram, the sum of perpendicular periodic frequencies in the final density field's Fourier transform was calculated. This serves as a coarse estimate of perpendicular order, effectively only useful to distinguish between films with some degree of perpendicular order and films with none. In practice, this is perfectly adequate as the vast majority of results exhibiting parallel morphologies are unambiguous with no perpendicular order whatsoever. The results of this study are shown in figure 2.7.

Evaporation Rate Effects

In the previous section, we determined that there existed conditions which were amenable to initiating a perpendicular ordering front in asymmetric copolymer systems provided the evaporation rate were large enough. The results showed a dependence on both evaporation rate and effective surface conditions - essentially degree of enthalpic surface preference for the minority block. Figure 2.8 provides snapshots from simulations at the same surface conditions, but where one simulation at a high evaporation rate resulted in a perpendicular ordering front while the other, at a lower evaporation rate, did not. This is an essential result of our simulation effort which demonstrates that the evaporation rate can explain the generation of a sustained perpendicular ordering front as an independently controlled parameter. The two simulations were run with identical starting configurations and system parameters, with the obvious exception of evaporation rate. One theory for why perpendicular fronts would form under rapid evaporation conditions hinges on the idea that there

is a polymer mobility gradient through the film due to the solvent concentration profile[27]. While technically ρ-dependent, our polymer mobilities are very weakly spatially dependent compared to the typical exponential models used in the paper. It is of course necessary to acknowledge that this is only significant provided our results transfer to the 3D cylinder-forming systems as expected.

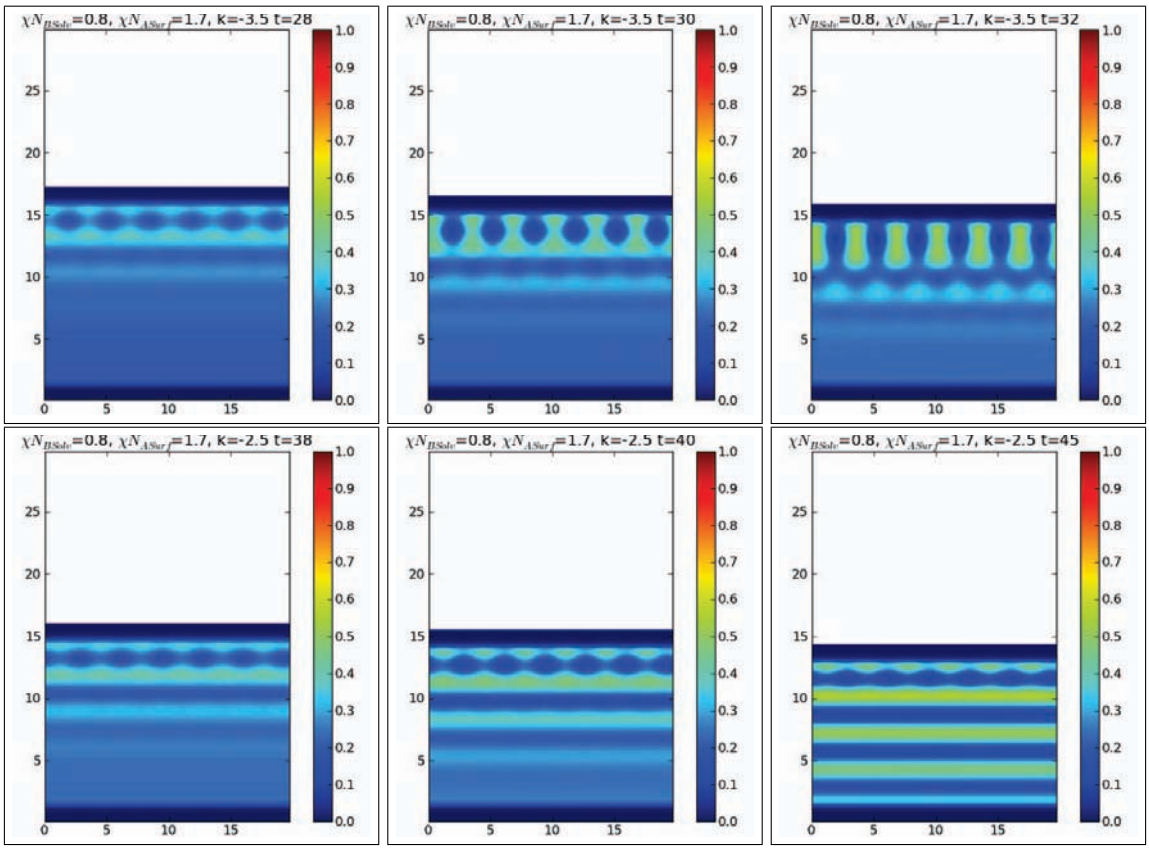

Figure 2.8. Comparison between successful nucleation of a perpendicular ordering front and a simulation whose conditions were outside the region of perpendicular order indicated in figure 2.7. Both simulations exhibit a slight $L_{\|}$ wave from the surface along with slight "post" formation at the surface. In the failed (bottom) trajectory, the preferentiality of the surface succeeded in damping the post formation, leading to parallel morphology. Time increases left→right, successful trajectory is in row 1, unsuccessful trajectory (k=-2.5) in row 2.

References

[1] http://www.cems.umn.edu/research/morse/code/pscf/home.php.

[2] http://dakota.sandia.gov/index.html

[3] VE Badalassi, HD Ceniceros, and S. Banerjee. Computation of multiphase systems with phase field models. *Journal of computational physics*, 190(2):371–397, 2003.

[4] Hector D. Ceniceros and Glenn H. Fredrickson. Numerical solution of polymer self-consistent field theory. *Multiscale Modeling & Simulation*, 2(3):452, 2004.

[5] David Chandler. *Introduction to Modern Statistical Mechanics*. Oxford U-Press, 1987.

[6] Henry Cohn and Abhinav Kumar. Algorithmic design of self-assembling structures. *P Natl Acad Sci Usa*, 106(24):9570–9575, 2009.

[7] Hany B Eitouni and Nitash P Balsara. Thermodynamics of Polymer Blends. In James E Mark, editor, *Physical Properties of Polymers Handbook*, pages 339–356. Springer, New York, March 2007.

[8] Christopher Forrey, K.G. Yager, and S.P. Broadaway. Molecular Dynamics Study of the Role of the Free Surface on Block Copolymer Thin Film Morphology and Alignment. *ACS nano*, (4):2895–2907, 2011.

[9] J. G. E. M. Fraaije. Dynamic density functional theory for microphase separation kinetics of block copolymer melts. *The Journal of Chemical Physics*, 99(11):9202, 1993.

[10] G H Fredrickson and F S Bates. Dynamics of Block Copolymers: Theory and Experiment. *Annual Review of Materials Science*, 26(1):501–550, August 1996.

[11] Glenn Fredrickson. *The Equilibrium Theory of Inhomogeneous Polymers*. Oxford U-Press, 2006.

[12] Glenn H Fredrickson, Venkat Ganesan, and F Drolet. Field-theoretic computer simulation methods for polymers and complex fluids. *Macromolecules*, 35(1):16–39, 2002.

[13] Enrique D Gomez, Ashoutosh Panday, Edward H Feng, Vincent Chen, Gregory M Stone, Andrew M Minor, Christian Kisielowski, Kenneth H Downing, Oleg Borodin, Grant D Smith, and Nitash P Balsara. Effect of Ion Distribution on Conductivity of Block Copolymer Electrolytes. *Nano Lett*, 9(3):1212–1216, 2009.

[14] Eungnak Han, Karl O. Stuen, Melvina Leolukman, Chi-Chun Liu, Paul F. Nealey, and Padma Gopalan. Perpendicular Orientation of Domains in Cylinder-Forming Block Copolymer Thick Films by Controlled Interfacial Interactions. *Macromolecules*, 42(13):4896–4901, July 2009.

[15] X. Hu, D. N. Beratan, and W. Yang. *J. Chem. Phys.*, 131:154117, 2009.

[16] HP Huinink, JCM Brokken-Zijp, MA Van Dijk, and GJA Sevink. Asymmetric block copolymers confined in a thin film. *The Journal of Chemical Physics*, 112(5):2452, 2000.

[17] Kyozi Kawasaki and Ken Sekimoto. Dynamical theory of polymer melt morphology. *Physica A: Statistical and Theoretical Physics*, pages 349–413, 1987.

[18] S.H. Kim, M.J. Misner, T. Xu, M. Kimura, and T.P. Russell. Highly oriented and ordered arrays from block copolymers via solvent evaporation. *Advanced Materials*, 16(3):226–231, February 2004.

[19] P Mansky, TP Russell, and CJ Hawker. Ordered diblock copolymer films on random copolymer brushes. *Small*, 9297(97):6810–6813, 1997.

[20] M W Matsen. Phase-Behavior of Block-Copolymer Homopolymer Blends. *Macromolecules*, 28(17):5765–5773, 1995.

[21] M W Matsen. Fast and accurate SCFT calculations for periodic block-copolymer morphologies using the spectral method with Anderson mixing. *Eur Phys J E*, 30(4):361–369, 2009.

[22] M W Matsen and F S Bates. Block copolymer microstructures in the intermediate-segregation regime. *J Chem Phys*, 106(6):2436–2448, 1997.

[23] MW Matsen and M Schick. STABLE AND UNSTABLE PHASES OF A DIBLOCK COPOLYMER MELT. *Phys Rev Lett*, 72(16):2660–2663, 1994.

[24] N. M. Maurits and J. G. E. M. Fraaije. Mesoscopic dynamics of copolymer melts: From density dynamics to external potential dynamics using nonlocal kinetic coupling. *The Journal of Chemical Physics*, 107(15):5879, 1997.

[25] J. Nocedal and S. J. Wright. *Numerical Optimization*. Springer, 2000.

[26] D Petera and M Muthukumar. Self-consistent field theory of diblock copolymer melts at patterned surfaces. *The Journal of chemical physics*, 109(12), 1998.

[27] William A. Phillip, Marc A. Hillmyer, and E. L. Cussler. Cylinder Orientation Mechanism in Block Copolymer Thin Films Upon Solvent Evaporation. *Macromolecules*, 43(18):7763–7770, September 2010.

[28] William A. Phillip, Brandon O'Neill, Marc Rodwogin, Marc A. Hillmyer, and E. L. Cussler. Self-Assembled Block Copolymer Thin Films as Water Filtration Membranes. *ACS Applied Materials & Interfaces*, 2(3):847–853, March 2010.

[29] M. Rechtsman, F. Stillinger, and S. Torquato. *Phys. Rev. E*, 73:011406, 2006.

[30] JU Sommer and Alexander Hoffmann. Block copolymer films between neutral walls: A Monte Carlo study. *The Journal of chemical physics*, 111(8):3728–3732, 1999.

[31] Jianhui Song, Yunqi Li, Qingrong Huang, Tongfei Shi, and Lijia An. Monte Carlo simulation on symmetric ABA/AB copolymer blends in confined thin films. *The Journal of chemical physics*, 127(9):094903, September 2007.

[32] Salvatore Torquato. Inverse optimization techniques for targeted self-assembly. *Soft Matter*, 5(6):1157–1173, 2009.

[33] David M. Trombly. Self-Assembly of Diblock Copolymer on Substrates Modified by Random Copolymer Brushes. *Macromolecules*, 25(24):6341–9881, December 2011.

[34] Mesfin Tsige. Molecular dynamics study of the evaporation process in polymer films. *Macromolecules*, 19(9):1405, September 2004.

[35] C A Tyler and D C Morse. Orthorhombic Fddd network in triblock and diblock copolymer melts. *Phys Rev Lett*, 94(20):208302, 2005.

[36] Mathias Ulbricht. Advanced functional polymer membranes. *Polymer*, 47(7):2217–2262, March 2006.

[37] Feng Wang, Michael Hickner, YS Kim, and TA Zawodzinski. Direct polymerization of sulfonated poly (arylene ether sulfone) random (statistical) copolymers: candidates for new proton exchange membranes. *Journal of Membrane*, 197:231–242, 2002.

[38] M. Wang, X. Hu, D. N. Beratan, and W. Yang. *J. Am. Chem. Soc.*, 128, 2006.

[39] Qiang Wang, Paul F. Nealey, and Juan J. de Pablo. Monte Carlo Simulations of Asymmetric Diblock Copolymer Thin Films Confined between Two Homogeneous Surfaces. *Macromolecules*, 34(10):3458–3470, May 2001.

DISTRIBUTION:

1	MS 0899	Technical Library, 9536 (electronic copy)
1	MS 0359	D. Chavez, LDRD Office, 1911

Sandia National Laboratories